Design and Processing of Multi-phase High Entropy Alloys

A Thesis

by

Amin Radi

Submitted to the

Graduate School of Sciences and Engineering
In Partial Fulfillment of the Requirements for
the Degree of

Master of Science

in the
Department of Mechanical Engineering

Özyeğin University
January 2022

Design and Processing of Multi-phase High Entropy Alloys

Approved by:

Assoc. Prof. Dr. Güney Güven Yapıcı
Advisor, Head
Department of Mechanical Engineering
Özyeğin University

Asst. Prof. Dr. Altuğ Melik Başol
Department of Mechanical Engineering
Özyeğin University

Asst. Prof. Dr. Mehmet İpekoğlu
Department of Mechanical Engineering
Turkish-German University

Date Approved: 06 January 2022

DEDICATION

To

Whom is looking for beyond

And

What makes those possibilities happen

Way of thinking!

ABSTRACT

The multi-principal element alloys (MPEAs) known as high- and medium-entropy alloys possess promising properties due to their highly distorted atomic crystal structures. Employing multi-elements as principal elements has enabled a new platform for novel alloy designs and fabrications. Adding other phases as a heterogeneous phase in MPEAs structures can boost the mechanical behavior. Therefore, the heterogeneous MPEAs address the strength-strain trade-off in most of the conventional alloys.

In this thesis, the microstructural evolution and mechanical behavior of two novel heterogeneous high-entropy alloys (HEA) are investigated through thermo-mechanical processing. Using the CALPHAD approach the compositions have been confirmed and subsequently cast. The homogenized samples for both compositions possessed a single-phase uniaxed face centered subic (FCC) structure with high ductility. Possessing high ductility levels in the homogenized condition enabled us to apply high thickness reductions via rolling at room temperature without crack propagation from edges.

This study confirms that the sigma phase contribution becomes more significant in the microstructure at higher annealing temperatures. However, the body centered cubic (BCC) phase contribution as a suitable hard-domain becomes less with increasing the annealing temperature. As such, a systematic approach to investigate the effects of the sigma phase and degree of recrystallization on the microstructure and mechanical behavior of the HEAs is presented.

In addition, samples subjected to annealing exhibit transformation-induced plasticity (TRIP) under plastic deformation. Results show that the sigma phase can limit the TRIP

mechanism in the alloy system since the TRIP-assisted BCC phase is decreased with increased sigma phase present in the microstructure. As such, the designed TRIP-assisted multi-phase HEA enables a combination of 1 GPa yield strength and about 10% of strain at failure for the optimum condition of post-rolled annealed at 750 ℃ for 30 minutes samples. Moreover, this work introduces a novel high strength HEA with proposing a proper combination of homogenization, rolling, annealing, and aging sequences and details for this composition.

ÖZET

Yüksek ve orta entropili alaşımlar (YEA) olarak bilinen çoklu element alaşımlar (MPEA), yüksek seviyede çarpılmaya uğramış kristal yapıları nedeniyle pratikte umut vadeden özelliklere sahiptir. Çoklu element yapılarının, ana elementler olarak kullanılması, yeni alaşım tasarımları ve bunların üretimi için yeni bir platform sağlamaktadır. MPEA bir yapıya eklenen başka bir heterojen faz, bu alaşımların mekanik özelliklerinin gelişmesini sağlamaktadır. Bu nedenle, heterojen MPEA'lar, geleneksel alaşımların çoğunda görülen mukavemet-gerinim takasını ele almaktadır.

Bu tezde, iki yeni heterojen yüksek entropi alaşımının (HEA) mikro yapıdaki değişimleri ve mekanik özellikleri, termo-mekanik prosesler ile incelenmiştir. CALPHAD kullanılarak alaşımların bileşimi kontrol edilmiş ve doğrulanmıştır. Buna göre alaşımların döküm işlemi gerçekleştirilmiştir. Homojenize edilen numunelerin, yüksek sünekliğe sahip, tek fazlı ve eş eksenli yüzey merkezli kübik (YMK) yapıya sahip olduğu gözlemlenmiştir. Alaşımların sahip olduğu yüksek süneklik özelliği, oda sıcaklığında uygulanan haddeleme işlemi sırasında herhangi bir çatlak oluşumu meydana gelmeden malzeme kalınlığının daha fazla azaltılabilmesini sağlamıştır.

Bu çalışma, daha yüksek tavlama sıcaklıklarında mikro yapıda bulunan sigma fazının etkisinin daha önemli hale geldiğini doğrulamaktadır. Ancak, daha sert yapıda olan hacim merkezli kübik (HMK) fazının katkısı, artan tavlama sıcaklığının ile ters orantılı olarak azalmıştır. Bu çalışmada, sigma fazının ve rekristalizasyon derecesinin YEA'nın mikroyapı gelişimi ve mekanik özellikleri üzerindeki etkileri incelenmiştir.

Bunlara ek olarak, tavlama ısıl işlemi uygulanan numuneler, plastik deformasyon altında dönüşüm kaynaklı plastisite (TRIP) davranışı sergilemektedir. Sonuçlar incelendiğinde sigma fazının TRIP mekanizmasını sınırlandırdığı görülmüştür. Keza TRIP destekli HMK fazı sigma fazı arttıkça düşüş göstermektedir. Bu nedenle, bu çalışmada tasarlanan TRIP destekli, çok fazlı YEA, 30 dakika 750°C'de tavlanan numunelerde akma mukavemeti 1 GPa olarak gözlenmiş ve kopma noktasında yaklaşık %10 gerinim elde edilen bir alaşım kombinasyonu sağlanmıştır. Ayrıca, bu çalışma homojenleştirme, haddeleme, tavlama ve yaşlandırmanın uygun bir kombinasyonunu önererek yüksek mukavemete sahip yeni bir HEA sunar.

ACKNOWLEDGEMENTS

I would like to thank my mother who dedicated her life to support me. I deeply thank her for all her sacrifices and dedication.

I would like to thank my brother, for his nonstop support, kindness, and help.

I would like to thank my supervisor, Prof. Dr. Güney Güven Yapıcı, for his precious guidance and support throughout my studies and research work.

I would like to thank our responsible of the manufacturing laboratory, Mr. Ulaş Yıldırım, for his contributions in this work and also my colleagues in the MEMFIS group, Ali Hosseinzade-Ghobadlue, S.Veghar Seyedmohammadi, Canay Demir, and my colleague Dr. Seyed Vahid Sajadifar at the University of Kassel for their great help and valuable time. Special thanks go to my best friend Peyman Asghari-Rad who has made valuable help and suggestions in this research work.

I would like to thank my M.Sc. committee members, Asst. Prof. Altuğ Melik Başol and Asst. Prof. Mehmet İpekoglu for their guidance and attention to this study.

TABLE OF CONTENTS

DEDICATION III

ABSTRACT IV

ÖZET VI

ACKNOWLEDGEMENTS VIII

LIST OF TABLES XIII

LIST OF FIGURES XIV

CHAPTER I 1

INTRODUCTION 1

1.1 Motivation 1

1.2 Research objectives 3

1.3 Work Summary 3

1.4 Research questions 4

CHAPTER II 6

PREVIOUS WORK 6

2.1 Introduction to Multi-principal Element Alloys 6

2.2 Strengthening Mechanisms 6

2.2.1 Grain Boundary Strengthening Mechanism 7

2.2.2 Back-Stress Effect 9

2.3 Thermodynamics of Multi-Principal Element Alloys (MPEAs) 13

2.3.1 The effect of entropy contributions on phase stability in binary random solid solutions 13

2.3.2 Single Phase MPEA 15

2.4 Heterogeneous MPEA 17

2.5 Sigma Phase Effect in DP-MPEAs 21

2.6 Transformation Induced Plasticity (TRIP) 23

2.7 Effect of Elements in TRIP Mechanism 24

2.8 Annealing Twins 25

2.9 Empirical Parameters: Valance Electron Concentration (VEC) 27

CHAPTER III 32

EXPERIMENTAL METHODS 32

3.1 Selecting the composition and general design concept 32

3.1.1 The VEC calculations for 1st composition 34

3.1.2 Thermodynamical Based Simulation 37

3.2 Heat treatment details for 1st composition 39

3.2.1 Selecting Post-annealing Temperature 39

3.2.2 Selecting Post-annealing Duration 41

3.3 Thermo-mechanical processing for 1st composition 42

3.3.1 Vacuum Induction Melting (VIM) 42

3.3.2 Homogenization 44

3.3.3 Plastic Deformation 45

3.3.4 Post-annealing processes 47

3.4 Theoretical Calculations for 2nd composition 48

3.4.1 The VEC calculations 48

3.4.2 Thermodynamic Based Simulation in 2nd composition 51

3.5 Thermomechanical processing details for 2nd composition 52

3.6 Microstructural Characterization 54

3.6.1 X-ray diffraction analysis 54

3.6.2 Scanning Electron Microscopy (SEM) 54

3.6.3 Electron backscatter diffraction (EBSD) 54

3.6.4 Transmission Electron Microscopy (TEM) analysis 55

3.7 Mechanical Behavior Characterization 56

3.7.1 Vickers microhardness 56

3.7.2 Tensile studies 57

CHAPTER IV 59

RESULTS AND DISCUSSIONS 59

4.1 Initial microstructures 59

4.2 Microstructural evolution during post-deformation annealing 61

4.2.1 XRD and EBSD analysis 61

4.2.2 Elemental Mapping 66

4.2.3 Kernel average misorientation (KAM) analysis 68

4.2.4 TEM Analysis 70

4.3 Mechanical properties 73

4.4 Analysis of Structure-Property Relations 77

4.5 Mechanical behavior studies for 2nd composition 78

CHAPTER V 81

CONCLUSION 81

FUTURE WORKS 82

BIBLIOGRAPHY 83

VITA…… 95

LIST OF TABLES

Table 1. Entropy distribution with regards to the number of different elements. 15

Table 2. MPEAs composition and their atomic crystal structure with related atomic and thermodynamical calculated amounts. 20

Table 3. Elemental data 31

Table 4. The values of Hmix (kJ/mol) calculated by miedema's model for atomic pairs between elements for 1st composition. 35

Table 5. Nominal composition and cast ingot composition. 43

Table 6. The values of Hmix (kJ/mol) calculated by miedema's model for atomic pairs between elements for 2nd composition. 49

Table 7. Nominal composition and cast ingot composition. 53

LIST OF FIGURES

Figure 1. Schematic representing the (a) grain boundary formation due to atoms interaction of two lattices with two different atomic crystal orientations and (b) dislocation migration to grain boundaries regarding the grain sizes. 8

Figure 2. (a) the Matthews critical thickness concept and (b) the Frank-Read source operation in a grain. 9

Figure 3. Different stages of heterogeneous microstructure under plastic deformation (a) both hard and soft domains are in the elastic region, (b) soft domain is in the plastic region and doing transformation induced plasticity (TRIP) and the hard domain is in the elastic region, (c) both the hard domain and soft domains are in the plastic region. 11

Figure 4. Schematic presenting the GNDs and caused forward stress in the hard domain and back stress in the soft domain. 13

Figure 5. Statistics of published papers in multi-principal element alloys (MPEAs), the orang graph is representing whole published papers, the blue graph is illustrating the MPEA papers published in single-phase MPEAs from 2004 to 2019. 16

Figure 6. Processing methods (a) High-Pressure Torsion (HPT), (b) Rolling, and (c) Equal Channel Angular Pressure (ECAP). 18

Figure 7. Schematic representing different stages during elastic and plastic regions and TRIP mechanism involved stages. 23

Figure 8. Schematic representing the twin structure and its sequence in an FCC atomic crystal structure. 26

Figure 9. The schematic is illustrating the contribution effect of different atoms with different atomic radii on the distortion of the atomic crystal structure. 28

Figure 10. Schematic representing the boundary conditions for FCC, BCC, and FCC-BCC atomic crystal structures. 33

Figure 11. Calculated phase diagram for the 25Ni-30Cr-30Fe-10Mn-5Co at% at the ThermoCalc thermodynamic software.....38

Figure 12. Schematic of the pre-step cube for understanding the thermomechanical behavior. 40

Figure 13. Microhardness results for post-roll annealing at 750℃ for 60 minutes (blue), 30 minutes (red), 15 minutes (black). 42

Figure 14. Casting and thermal process details (a) casting die's characteristics, (b) casting machine, (c) vacuum tube furnace. 44

Figure 15. Schematic representing the rolling process and its related parameters and characteristics.....46

Figure 16. Calculated phase diagram for the 32Ni-25Fe-25Co-6Cr-6Ti-6Mo at% at the ThermoCalc thermodynamic software (due to sluggish diffusion rate at lower temperatures, the present phases at temperatures lower than 550 ℃ were eliminated from the calculated phase diagram). 51

Figure 17. Schematic representing the Vickers microhardness test with related standards for avoiding wrong data and decreasing the errors. 56

Figure 18. Schematic representing the characteristics of the dog-bone shape tensile sample, points 1 and 2 are illustrating the regions for EBSD characterization.....58

Figure 19. (a) The XRD patterns of as-received (blue) and 80% rolled (red) specimen, Phase map of (b) as-received and (c) rolled sample, EBSD inverse pole figure (IPF) map of (d) as-

received sample and (e) rolled sample, Kernel average misorientation (KAM) maps of (f) as-received and (g) rolled samples. 60

Figure 20. (a) The XRD patterns of the samples annealed at 750 ℃ (yellow), 800 ℃ (blue), and 850 ℃ (purple), EBSD phase maps of the samples annealed at (b) 750 ℃ taken from the grip part, (c) 750 ℃ taken from the tip part, (d) 850 ℃ taken from the grip part, (e) 850 ℃ taken from the tip part, and (f) 800 ℃ taken from the grip part. 63

Figure 21. Schematic illustration of microstructural evolution in the rolled samples annealed at 750 ℃ and 850 ℃ during tensile deformation. 65

Figure 22. (a) The SEM-SE micrograph of the 850 ℃ specimen with (b) corresponding SEM-EDS maps representing the Cr-rich regions as sigma phases. 66

Figure 23. TEM micrographs for 850 ℃ post annealed sample at the zone without the TRIP mechanism (a and b) are representing TEM-micrographs including FCC, B2, and sigma phases, (c) HRTEM graph from the sigma phase, (d) SAED pattern of sigma phase, and (e) schematic of BCT for sigma phase. 67

Figure 24. The Kernel average misorientation (KAM) maps of the samples annealed at (a) 750 ℃ taken from the grip part, (b) 750 ℃ taken from the tip part, (c) 850 ℃ taken from the grip part, (d) 850 ℃ taken from the tip part, (e) 800 ℃ taken from the grip part, and (f) the rolled specimen. 69

Figure 25. Annealing twins represented in fully recrystallized grains of 850 ℃ sample free of dislocations and schematic illustrating the present planes and directions in annealing twin in an FCC lattice. 71

Figure 26. Transmission Electron Microscopy (TEM) micrograph of 850C (a) grip part possessing B2 crystal structure and (b) TRIP assisted zone (gage part) possessing BCC crystal structure with their related SAED pattern. 72

Figure 27. (a) engineering stress-strain graph, (b) true stress-strain graph, and (c) strain hardening rate (SHR) curves of the present HEA at different processing conditions. 74

Figure 28. (a) Engineering stress-strain and (b) true stress-strain and strain hardening rate (SHR) curves of the present HEA at different processing conditions, and fracture surface of the samples at different conditions of (c and d) as-received, (e and f) annealed at 750 ℃, and (g and h) annealed at 850 ℃. 76

Figure 29. (a) engineering stress-strain and (b) true stress-strain for as-received, rolled, and multiple annealing at 900 ℃ with the durations of 5, 10, 15, 20, 25, and 30 minutes followed by 180 minutes aging at 650 ℃ for 2nd composition. 79

CHAPTER I

INTRODUCTION

1.1 Motivation

Since the development of the first alloys by humans, alloys have been evolved to provide engineered materials with improved mechanical and chemical characteristics. These engineered materials are a vital part of materials that have been designed and fabricated artificially to enable groundbreaking mechanical characteristics, e.g., simultaneous high strength and ductility for various usages and industrial applications considering different engineering and safety aspects.

Therefore, the advancement of high-performance alloy compositions possessing high strength and ductility is a highly attractive field of science and technology. The stress-strain trade-off has always challenged the researchers since the strengthening of the alloy via conventional strengthening methods leads to decreasing the strain values. On the other side, increasing ductility can shift the stress to lower values. This behavior is known as the stress-strain trade-off. This said, designing alloys using conventional concepts and methods restricts the discovery and fabrication of new alloys with advanced characteristics.

The concept of Multi-Principal Elements (MPE) materials, generally known as high entropy alloys, is a different and new alloy design method that enables a new platform for material design with advanced characteristics, offering broader opportunities to discover many novel alloys with extraordinary characteristics.

In 2004, two different research groups simultaneously announced the Multi-Principal Element Alloys (MPEAs) with high strain value at Giga Pascal (GPa) levels [1,2]. After the introduction of the Cantor alloys with a single-phase face-centered cubic (FCC) with an equiatomic combination of five elements of Fe, Ni, Cr, Co, and Mn, a huge part of research in developing alloys concentrated on this composition.

Since the first introduction of MPEAs, numerous alloys using this multi-principal alloy concept have been developed in a single phase of FCC atomic crystal structure. Soon after, researchers developed new MPEAs with multi-phase microstructures known as heterogeneous MPEAs. This strategy enables researchers to overcome strength-ductility synergy. Heterogeneities such as variation in the crystal structure, composition, grain sizes, and many other characteristics can make the alloys benefit from different mechanical behaviors of contributed parts.

However, it should be noted that fabricating heterogeneity as hard/soft domains in the microstructure will not always result in improved strength-ductility synergy. The introduced morphology, i.e., size, fraction, and distribution, of hard/soft domains are determinative in the final mechanical behavior. Design and fabrication of a delicate system that contains all optimum parameters is not an easy task because it requires extensive theoretical analysis and experimental validations. Although using brute-force optimization of microstructural characteristics and manufacturing parameters could, in principle, work for some cases in solving stress-strain trade-offs, this is not a universal technique and will not provide a solution for all material design problems we may deal with [3].

Extensive studies have been done on the effect of each parameter involved in the design and fabrication process of conventional alloys. However, there are only a limited

number of similar studies on heterogeneous MPEAs. Therefore, introducing a perfect design path for heterogeneous MPEAs remains to be discovered. More research works are needed to be done by concentrating on developing a solid and universal way in the design and fabrication of heterogeneous MPEAs with high-strength ductile alloy systems.

1.2 Research objectives

The main goal of this work is to design, fabricate, and study the novel heterogeneous MPEA compositions and provide a deep view of the plasticity mechanisms (including TRIP) in the interaction of different present phases and their distribution and morphology. These goals have been achieved through the following steps:

1. Investigating the most appropriate heterogeneous MPEAs and selecting the proper elements to work with.
2. Investigating, simulating, and running the possible phase diagrams originated by the selected compositions.
3. Designing the most proper path including homogenization temperature and time, applied cold work level, reduction temperature, post-deformation annealing temperature and time, aging temperature, and duration for causing target micro and nano-structured heterogeneous alloys after casting.
4. Investigating the mechanical behavior at room temperature (RT) and its related microstructural characteristics.

1.3 Work Summary

In the current study, multiple heterogeneous multi-principal element alloys (MPEAs) have been designed, fabricated, and studied throughout a systematic process. Microhardness

tests have been done in all required steps for having a better understanding of the materials' stage before any advanced mechanical tests. Annealing and aging temperature and time have been selected based on the microhardness tests. Isothermal uniaxial tensile tests were employed for the prepared dog-bone-shaped samples. This test was run under strain rates of 0.015 s^{-1} to study the effect of different microstructures on the mechanical behavior of the alloy.

The fabricated microstructure for 1st composition at 750 ℃ showed a superior YS, UTS, with acceptable strain to failure, and uniform elongation of 1 GPa, 1.075 GPa, 10%, and 5%, respectively. It has been proved how the mechanical behavior of the alloy is affected by the sigma phase. In addition, the relation of Transformation Induced Plasticity (TRIP) with characteristics of the present sigma phase in the microstructure was studied in detail. In addition, the introduced microstructure in the 2nd composition via 15 min-900 ℃ annealing followed by 180 min-650 ℃ aging revealed a superior YS, UTS, and ductility of 1.283 GPa, 1.457 GPa, and 20%, respectively.

1.4 Research questions

In general, the following questions have been addressed throughout this work, shedding light on some of the unanswered questions:

- What are the microstructural characteristics of the new heterogeneous MPEAs in as-received, rolled, different annealing, and aging conditions?
- How can different approaches in the annealing step affect the mechanical behavior?

- Can the fabrication of heterogeneous structures boost mechanical behavior? If yes, what are the mechanisms present in these approaches, and what is their contribution in intensifying the mechanical behavior?
- What is the effect of the various phases in the microstructures of the designed MPEAs? How can they affect the mechanical behavior? And is there any acceptable amount of a certain phase for boosting the mechanical behavior via dislocation motion and/or other mechanisms such as TRIP?

CHAPTER II

PREVIOUS WORK

2.1 Introduction to Multi-principal Element Alloys

Multi-principle element alloys (MPEAs) have increasingly been represented as candidates to cover demands for materials with superior mechanical behavior [4]. Overcoming the strength-ductility trade-off has been one of the controversial topics in modifying the alloys. High- and medium-entropy alloys (HEA and MEA) comprising several principle elements evoke great attention due to their unique mechanical and chemical behaviors [5,6]. The MPEAs were introduced in 2004, and since then, they have opened up new horizons in materials advancements [1,7,8].

The concept for this new approach in alloy design was to introduce baseless multi-elements alloys. The single-phase face-centered cubic (FCC) MPEAs possess low yield strength (YS) values with high ductility in the annealed condition at room temperature [9]. Multiple research has proven that possessing a single phase in an MPEA does not necessarily lead to higher stability, and as mentioned previously most of the time leads to moderate mechanical behaviors. Such characteristics presumably limit the potential usage of these alloys. Therefore, considerable research was conducted to introduce new microstructural designs and produce heterogeneous MPEAs to boost the mechanical properties [10,11].

2.2 Strengthening Mechanisms

The general concept of all strengthening mechanisms is decreasing the movement ability of the dislocation in the microstructure by introducing obstacles. The homogeneous

materials can be strengthened by methods like precipitation hardening, grain boundaries, and solid solution strengthening. However, introducing heterogeneity in the system is another efficient way. This kind of structure can primarily be introduced by causing variation in their crystal structure, chemical composition, stacking fault energy (SFE), and grain size variation [12,13].

Here, two main mechanisms that have the most contribution to this thesis work are explained in detail.

2.2.1 Grain Boundary Strengthening Mechanism

In general, materials can be modified in their strength properties via introducing homogeneous [14] and heterogeneous structures in the designed alloy [15]. The grain refinement (homogeneous) improves the mechanical behavior by increasing the density of grain boundaries as barriers against dislocation movement during plastic deformation [16] (see Figure 1a). In other words, with decreasing the grain sizes in the alloy microstructure, a lower number of dislocations can be introduced in the grains and can lead to a lower dislocation pile-up (pressure) at grain boundaries (Figure 1b).

Based on the Hall-Petch strengthening mechanism, decreasing average grain size leads to an increase in the hardness of the material. Therefore, the nanocrystalline materials should possess higher strength than those with coarser grain size. Materials based on their average grain size are divided into four main categories: Micron-Size Structure having a grain size of over $1\mu m$, Submicron Grains with a grain size of $500\ nm < d < 1000\ nm$, Ultra-fine Grains (UFGs) in the range of $100\ nm < d < 500\ nm$, Nano-Crystalline Grains with a grain size of less than $100\ nm$.

With such an approach the dislocations' ability to move into the next grains and density of dislocation at the grains drops sharply. Therefore, the strength of materials can be increased by a decrease in their grain sizes corresponding to $\sigma_y=\sigma_0+k_y d^{-1/2}$ (Hall–Petch equation). In Hall–Petch equation, σ_y is yield strength, σ_0 indicates the strength in a single crystal mode, k_y is constant, and d stands for grain size. In addition, hardness is evolved with $H_v = H_0 + k_y d^{-1/2}$ where the H_v is modified hardness, H_0 is hardness in a single crystal mode, k_y is constant, and d represents the average grain size after modification.

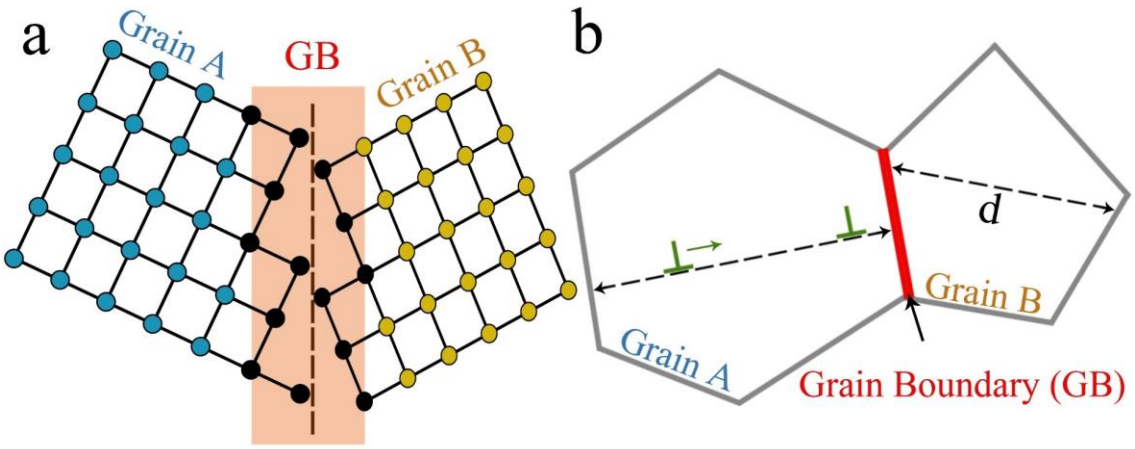

Figure 1. Schematic representing the (a) grain boundary formation due to atoms interaction of two lattices with two different atomic crystal orientations and (b) dislocation migration to grain boundaries regarding the grain sizes.

However, increasing the strength of the material by decreasing the average grain size is limited depending on the materials. In other words, after a specific grain size (around 30 nm), more decrease in the grain sizes does not increase the strength and it starts to behave against and material loses its superior mechanical behavior. At this point, the density of the grain boundaries is very high and the difference between the interior part of grains and their boundaries is unrecognizable. Therefore, there will be an extremely limited capability for

dislocations to be created and moved [17]. This behavior is known as the Inverse Hall-Petch effect and it has been proven by various experimental [18] and molecular dynamic (MD) simulation [19,20] research works.

On other hand, the dislocation production source and movement mechanism will be confined by decreasing the grain size to nanometer levels. For instance, Figure 2a is demonstrating the Matthews critical thickness concept [21] for a spiral and Frank-Read dislocation source [22] in a twisted epitaxial layer on a substrate, and Figure 2b is illustrating the Frank-Read source operation in a grain. It is shown that after a specific distance and diameter some particular mechanisms will be paralyzed, and they will be unable to produce and help in continuous plastic deformation processes and will negatively affect the mechanical behavior in the material.

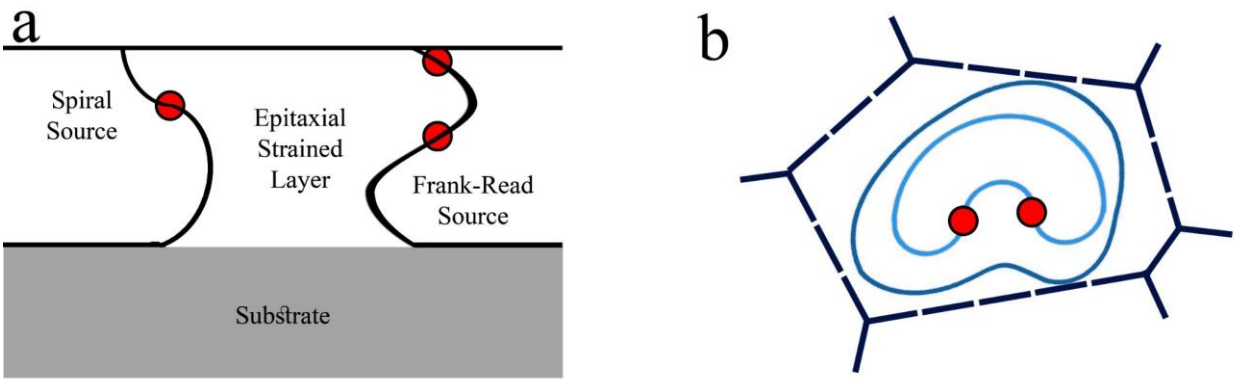

Figure 2. (a) the Matthews critical thickness concept and (b) the Frank-Read source operation in a grain [21,22].

2.2.2 Back-Stress Effect

The recent research works have shown that the conventional strengthening methods are not good enough in acquiring an excellent mechanical behavior. The conventional

mechanisms mainly lose one factor of high strength and/or high ductility at expense of increasing other (stress-strain trade-off). However, a heterogeneous approach seems a proper solution to conquer this common problem. These structures get their strength from hard-domain and ductility from soft-domain and lead to a strength-ductility synergy. This new strengthening approach is based on the concept of back-stress and forward-stress effect [23].

During deformation to failure, the deformation process can be divided into three main stages. As illustrated in Figure 3, both the hard and soft domains start a simultaneous elastic behavior. In this stage, there is no difference between the domains (Stage I Figure 3a), and both are in the elastic region. In the second stage, the soft domain is in its plastic zone and starts to produce dislocation and plastic behavior (Stage II Figure 3b). However, the hard domain still is in the elastic region and dislocations do not happen for this phase yet.

Due to this asynchronous behavior a mechanical incompatibility generates and leads to applying constraint on the soft domain due to inability in free deformation. Moreover, to keep a continuous strain across the interface, a level of strain gradients happens in the soft domain close to the phases' interface. In overcoming and accommodating the strain gradient and providing a simultaneous deformation ability between two domains, the soft domain starts to generate dislocations that are not produced in normal situations. The geometrically-necessary dislocations (GNDs) as a solution are proposed in such a scenario by the constrained microstructure [24].

The generated GNDs cause back-stress which is applied at long-range in the material in the opposite path to the applied force. The back-stress helps to strengthen the soft domain by interfering with the dislocations' movement and leads to delay in rupturing of the soft domain. By postponing failure in FCC phases, the hard domain starts the plastic deformation

(Stage III Figure 3c) and the alloy system initiates its simultaneous deformation in the plastic region [25,26].

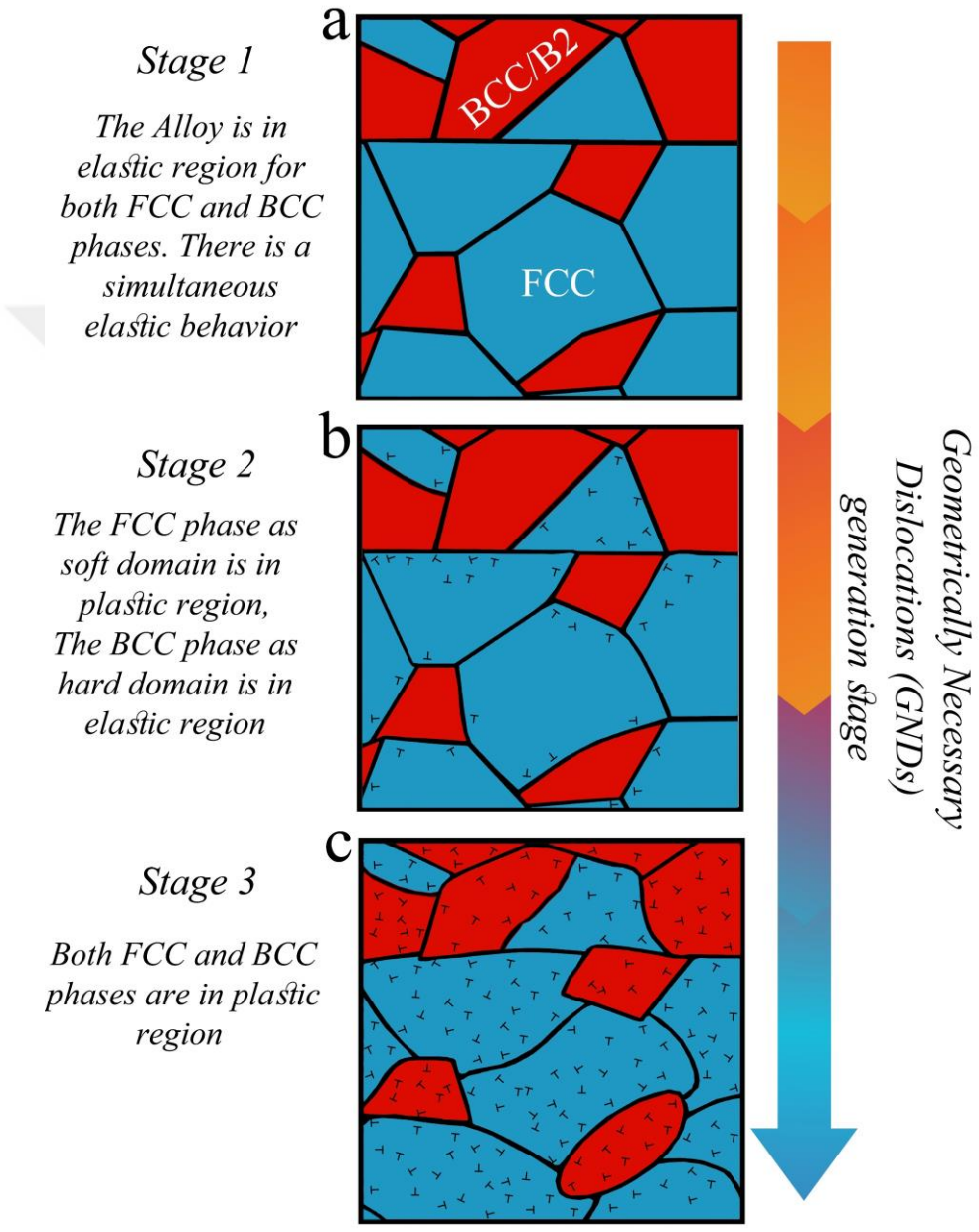

Figure 3. Different stages of heterogeneous microstructure under plastic deformation (a) both hard and soft domains are in the elastic region, (b) soft domain is in the plastic region and doing transformation induced plasticity (TRIP) and the hard domain is in the elastic region, (c) both the hard domain and soft domains are in the plastic region.

Besides the GNDs pile-up processes, generated GNDs evolve stress focusing on the boundaries (FCC-BCC interface) and BCC phase as hard domain begins yielding to adapt to this stress concentration. The stress concentration creates a stress zone in a similar path to the applied force, which is called forward stress. It means that the caused strength is not only initiated from back-stress since the system has forward stress too. These forward and backward stresses generated by GNDs creation and piling-up processes are initiated from hetero-deformation of the designed microstructure (Figure 4). Therefore, new concepts of hetero-deformation-induced (HDI) stress and HDI hardening can be introduced to define the back-stress and back-stress hardening [23]. Based on the literature the interaction of back-stress and forward stress and created HDI-stress and HDI-hardening are not clear yet and new research needs to be done to give a crystal-clear view of the whole mechanism.

By yielding at the interfaces, most probably, the system starts to stress and strain relaxation [27,28]. At the final stage, both soft and hard domains start the plastic deformation simultaneously, and higher withstand to plastic strain in the soft domain leads to strain partitioning. On other hand, the hard domain tolerates higher amounts of stress which result in stress partitioning (Stage III Figure 3c). In general, it can be told that a strain gradient is generated at the interface of soft and hard domains to ease the strain and stress partitioning, and boost strain hardening capability due to the back stress effect [29]. Since introducing this approach, the hard domain-soft domain heterogeneous microstructure seems the only way to improve the YS and strain instantaneously unlike conventional strengthening mechanisms.

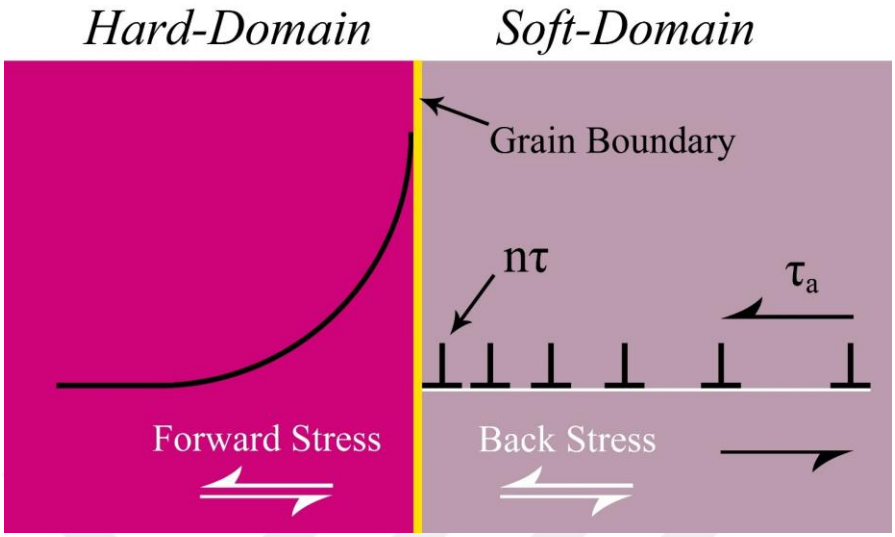

Figure 4. Schematic presenting the GNDs and caused forward stress in the hard domain and back stress in the soft domain.

2.3 Thermodynamics of Multi-Principal Element Alloys (MPEAs)

2.3.1 The effect of entropy contributions on phase stability in binary random solid solutions

Based on the designed alloy composition, MPEA can form a simple-phase solid solution, like FCC, BCC, and/or HCP phases more probably at higher temperatures. However, this can be expanded to lower temperatures in some cases. Due to thermodynamic laws, the system is trying to minimize the present Gibbs free energy (ΔG_{mix}) as much as possible to attain a stable or metastable equilibrium condition. Enthalpy (ΔH_{mix}) and Entropy (ΔS_{mix}) are associated with ΔG_{mix} at a specific temperature (T, expressed in Kelvin) by Eq. 1.

$$\Delta G_{mix} = \Delta H_{mix} - T\,\Delta S_{mix} \quad (1)$$

Eq. 1 shows that by increasing ΔS_{mix} and/or decreasing ΔH_{mix}, the total Gibbs free energy can be decreased. The entropy depends on four determining parameters of the configurational, magnetic dipole, vibrational, and electric randomness. Between these parameters, the configurational factor for MPEAs is higher due to multiple principal elements in comparison to conventional alloys. The Gibbs free energy with the contribution of enthalpy and entropy determines the phase stability in a system. The enthalpy is indicating the development of a stable solid solution and an unmixing situation can happen in higher enthalpy values. The contribution of the ΔS_{mix} in comparison to ΔH_{mix} is less important and it is used for determining the order-disorder status of the produced phases. However, at higher temperatures, the $T\Delta S_{mix}$ acts as a dominant factor and leads to the reason why the MPEA system tends to form a single-phase structure at higher temperatures [30].

Boltzmann's equation (2) is representing the configurational entropy for a specific system. The configurational entropy rises with the contribution of various elements.

$$\Delta S_{mix} = -R \sum_{i=1}^{n} c_i \ln c_i = R \ln N \tag{2}$$

By employing the mentioned equation (Eq. 2), the configurational entropy can be calculated for the equiatomic system (**Table *1***). The values have been calculated up to 13 different elements since, after this level, increasing the element's number makes a slight difference in total entropy. In addition, higher values in entropy effectively decrease the phases' presence possibility and increase the solubility of elements with different radii and characteristics.

Table 1. Entropy distribution with regards to the number of different elements.

	Low		Medium		High								
	0		1.1R		1.5R								
n	1	2	3	4	5	6	7	8	9	10	11	12	13
$\Delta S_{mix}/R$	0	0.69	1.1	1.39	1.61	1.79	1.95	2.08	2.2	2.3	2.4	2.49	2.57

2.3.2 Single Phase MPEA

Single-phase alloys are known as compositions that possess just one present phase of FCC, BCC, HCP, and/or other atomic crystal structure in the alloy system [31]. Phases in the thermodynamic software can be called in different names and proper care should be taken when dealing with these. For instance, the FCC phase in thermodynamic software is present as the Gamma phase and the sigma phase represents the BCT crystal structure.

In the single-phase MPEAs, after passing the melting temperature to lower amounts, the alloy stays in one single phase without degradation and introducing other phases in the microstructure. These kinds of alloys own limited mechanical and chemical behaviors. As shown in Figure 5, research work in this sort of MPEAs have grown very slowly, e.g., in 2019 only 146 paper has been published in this area which is a much lower number in comparison to the number of publications in the area of heterogeneous MPEAs [32].

The FCC-MPEAs have very ductile behavior, but their strength is not acceptable in most cases. On the other hand, the BCC- and HCP-MPEAs possess high strength with lower ductility. The Valence Electron Concentration (VEC) is one of the main parameters that can influence mechanical behavior. Therefore, by tailoring the VEC values the mechanical

behavior can be tuned. The FCC atomic crystal structure can dominate the alloy in modifying the mechanical behavior to more ductile behavior by adding elements with higher VEC amounts. However, by adding elements with lower VEC amounts the BCC phase gets more favored in the microstructure, and alloy shows higher strength.

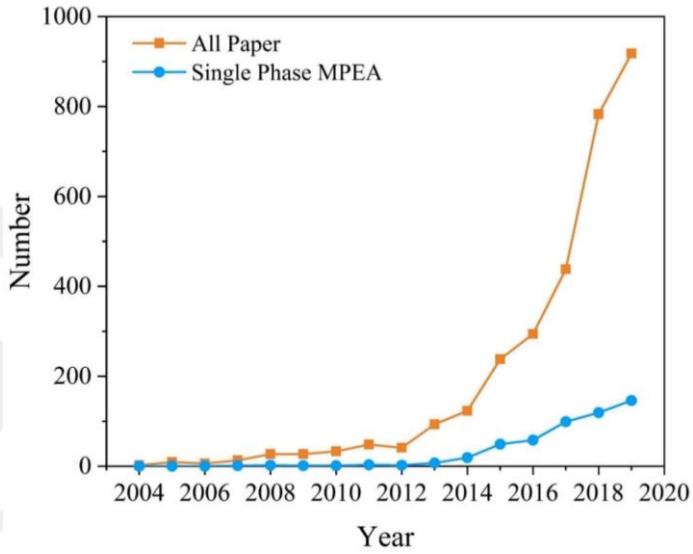

Figure 5. Statistics of published papers in multi-principal element alloys (MPEAs), the orang graph is representing whole published papers, the blue graph is illustrating the MPEA papers published in single-phase MPEAs from 2004 to 2019.

The VEC concept is acceptable when there is a solid solution. As mentioned previously, the presence of a multi-principal base in MPEAs makes these alloys vulnerable for single-phase formation. Therefore, the VEC definition for stabilizing different crystal structures is prominently valid for MPEAs and not for intermetallic structures and others. On the other hand, the factors of enthalpy, atomic size difference, and electronegativity are working against stabilizing the single phase. The VEC factor at higher temperatures is the determining factor since the entropy effect is high at higher temperatures. It must be

mentioned that nothing is solid in this conversation and the pointed roles can be evolved based on the situation.

Strategies in alloy design are adjusting these factors in a way that alloy shows a single phase at a higher temperature (for homogenization process) and multiple phases at a lower temperature (introducing heterogeneous microstructure).

2.4 Heterogeneous MPEA

Heterogeneity in the crystallographic texture of a designed alloy may enhance the mechanical behavior without applying any changes in the chemical composition of the base alloy. Various methods can be employed to generate a specific texture based on the considered final target. High-pressure torsion (HPT) [33] (see Figure 6a), Rolling [14] (see Figure 6b), and equal-channel angular pressing (ECAP) [34] (see Figure 6c) are three main manufacturing methods in modifying alloy structure in the micro-and nano-levels.

Deformation mechanisms can directly be influenced by the SFE of the understudied material [35]. The FCC-structured MPEAs with high SFE values have a low tendency to form twinning during plastic deformation [36]. The aforementioned characteristics provide a high potential for the FCC MPEAs to be processed via stated manufacturing processes with the least possibilities of initiating mechanical processing issues. According to previous research the FCC phases always possess a ductile behavior with low strength, however, the BCC phases are more strength with lower ductility. Therefore, having these two phases with completely different mechanical behavior can provide a mechanical behavior that owns strength besides ductility. The metastable dual-phase (DP) alloy systems consisting of face-center cubic (FCC) and body-centered cubic (BCC) phases have received significant

attention due to their mechanical behavior capabilities [37–39]. They possess higher meta-stability attributed to introducing a lower SFE phase in the alloy system.

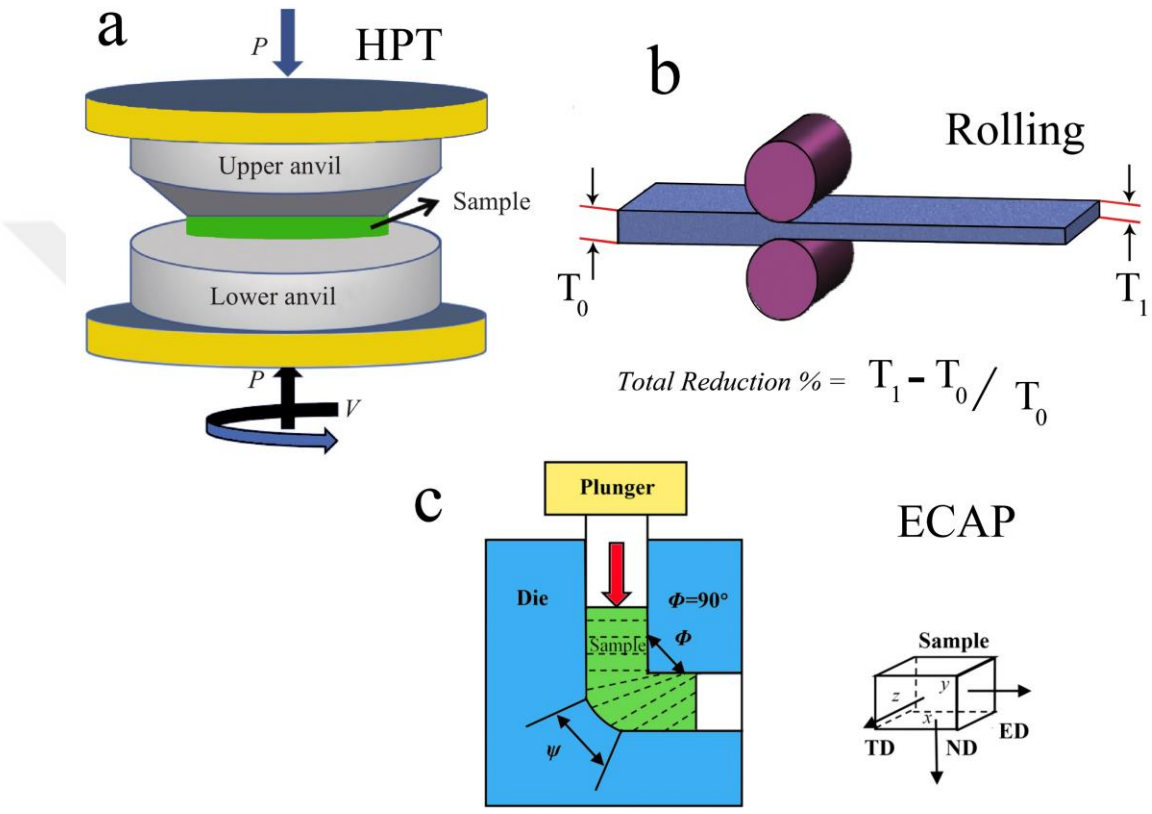

Figure 6. Processing methods (a) High-Pressure Torsion (HPT), (b) Rolling, and (c) Equal Channel Angular Pressure (ECAP).

For the first time, Tong et al. presented the $Al_xCoCrCuFeNi$ (x= 0 to 3.0 in molar ratio) with FCC-BCC atomic crystal structure. They showed how an atomic crystal structure in a specific MPEA can be altered by changing the chemical composition in very slight amounts [40]. After this breakthrough, multiple research works have been done in studying the mechanical behavior of dual-phase FCC-BCC structures [41], chemical behavior [42], phase evolution [43,44], and process effect in these DP-MPEAs [45]. The FCC-BCC

heterogeneous MPEAs have introduced fascinating mechanical, chemical, electrical, and numerous other unique behaviors to the world of designing materials with advanced characteristics. Recently in 2021, these alloys were studied for their oxidation behavior [46], magnetic behavior [47], and superior mechanical behavior [48] via employing cutting edge fabrication methods [49] and complicated chemical compositions [50].

Table 2 is representing a comprehending review of the chemical composition of some MPEAs and resulting atomic crystal structure. This table does not include all known FCC, BCC, FCC-BCC, BCC, and/or other contributions with Laves and intermetallic, however, it depicts the phase evolution under changing the contributed elements. The compositions are showing how with even a slight change in elements amount the present atomic crystal structure is altered. The ΔS_{mix} values are increasing with increasing the number of present elements in the system, e.g., with mixing 9 elements in $FeVMnCoCuNiCrTiAl_2$ composition the ΔS_{mix} value increases to almost 18.

In addition, it seems that a huge part of research works start with a ductile FCC base atomic crystal structure and shift to BCC structure. Therefore, this strategy is an acceptable approach in introducing a brand new MPEA alloy. The VEC values at maximum amounts are 10.5 and move to values up to 4.56 in a complete BCC phase structure. Plus, the calculated values altered easily even with adding amounts like 0.1 in atomic percent (at%).

Table 2. MPEAs composition and their atomic crystal structure with related atomic and thermodynamical calculated amounts.

Reference	*Composition*	*Phase*	ΔS_{mix}	δ	*VEC*
[51]	FeCoNiAl0.1Si0.1	FCC	10.87	2.95	8.66
	FeCoNiAl0.2Si0.2	FCC	11.75	4.02	8.35
	FeCoNiAl0.3Si0.3	FCC+BCC	12.32	4.76	8.08
	FeCoNiAl0.4Si0.4	FCC+BCC	12.32	4.76	8.08
[52]	CuCoNiZn	FCC	11.53	4.67	10.50
	FeNiCuCrAl	FCC+BCC	13.38	5.63	7.60
[53]	FeCoCrNi	FCC	11.53	0.29	8.25
[54]	FeCoCrNiPd	FCC	13.38	4.04	8.60
[55]	FeVCoCuNi	FCC	13.38	2.20	8.60
[56]	FeCoNiCrAl0.25	FCC	13.38	5.78	7.20
	FeCoNiCrAl0.5	FCC+BCC	13.15	4.60	7.67
[57]	FeNiCoCuCrTi0.5	FCC	14.70	4.82	8.36
	FeNiCoCuCrTi0.8	FCC+Laves	14.87	5.70	8.14
[58]	VTiTaNbAl0.2	BCC	12.57	3.85	4.67
	TiVTaNbAl0.5	BCC	13.15	3.74	4.56
[2]	FeCrCoNiCuAl0.3	FCC	14.43	3.42	8.47
	FeCrCoNiCuAl0.8	FCC+BCC	14.87	4.92	8.00
	FeCrCoNiCuAl1.3	FCC+BCC	14.85	5.69	7.60
	FeCrCoNiCuAl2.8	BCC	14.01	6.57	6.72
[59]	FeTiCrNiCoAl0.5	FCC+BCC+CoTi2+ FeTi	14.70	7.04	7.00
	FeTiCrNiCo	FCC+BCC+CoTi2	13.38	6.68	7.40
	FeTiCrNiCoAl1.5	FCC+BCC	14.78	7.29	6.38
[60]	FeVMnCoCuNiCrTi	BCC	17.99	6.27	6.60

	Al2				
	FeTiCrCoNiAl	BCC+BCC	14.90	7.22	6.67
[61]	FeCrCoNiAl	BCC	13.38	5.78	7.20
[62]	MoTaNbW	BCC	9.13	0.33	9.00
[63]	HfNbZr	BCC	9.13	5.00	4.33
[64]	FeNiCoCuCrAlSi	FCC+BCC	16.18	6.13	7.29
[65]	NiTiCoCuZnAl	FCC+BCC	14.90	6.91	7.33
[66]	FeNiCuCrMo	FCC+FCC+BCC	13.38	3.58	8.20
[67]	NbZrCrTiMO0.5Ta0.5	BCC+BCC+Laves	14.53	8.04	4.90

2.5 Sigma Phase Effect in DP-MPEAs

Thermomechanical processing of MPEAs can lead to the introduction of some other phases that can be negatively or positively affect the mechanical behaviors. The intermetallic sigma phase in MPEAs is one of those phases that can introduce unintentionally or intentionally based on the final goal. This chromium-rich (Cr-rich) phase usually precipitates at a higher temperature during fabrication steps. For example, in rolling and annealing at elevated temperatures, and in casting and welding processes. This phase possesses a base center tetragonal (BCT) atomic crystal structure and is brittle since it owns a limited slipe system during plastic deformation. Therefore, with introducing the sigma phase in the alloy microstructure there is a high possibility to decrease the mechanical behavior in MPEAs [68,69].

The sigma phase presence can be affected by changing the FCC (austenite) and/or BCC (martensite) stabilizers. For instance, nickel (Ni) as an austenite stabilizer can

profoundly decrease the presence probability of the sigma phase in the alloy microstructure. In other words, decreasing the nickel (Ni) can introduce more sigma at higher temperatures [70]. The MPEAs with a wide chemical composition range besides high contributed values of elements are vulnerable to introducing the sigma phase in their structures. Therefore, the sigma phase precipitation can effectively tune in MPEAs based on final mechanical behavior.

The intermetallic sigma phase presence can halt the grain growth in the recrystallization process because of Zenner pinning effect and can contribute to positive factors in tuning the final mechanical characteristics [70]. However, as mentioned before, the Cr-rich sigma phase is not acceptable in all situations, and in most cases, the negative point of the sigma phase can overcome the positive points [71,72]. The Cr-rich sigma phase was profoundly reported in multiple research works and was studied in detail to show how the sigma phase in different combinations can affect the other phases' contribution to microstructure and mechanical behavior of high and medium entropy alloys [73,74].

Knowing the generation mechanisms of the sigma phase for having a universal concept of possible mechanical and chemical characteristics is highly important. The sigma phase nucleates in two main areas: grain boundaries and grain interior. During the casting process, the sigma phase generates at grain boundaries, however, this intermetallic phase nucleates at grain interior during annealing processes [69]. The twin boundaries are other places that thermodynamically have higher energy in microstructure but this energy is not quite enough to make these regions possible zones for sigma phase initiation [75].

2.6 Transformation Induced Plasticity (TRIP)

The transformation-induced plasticity (TRIP), in general, can be defined as "… substantially enhanced plasticity under a phase evolution". In terms of the microstructural viewpoint, the TRIP mechanism can be described as the evolution of the austenite phase to the martensite phase under specific plastic deformation. By occurring the TRIP mechanism in the microstructure, the strength and ductility can be intensified simultaneously. The TRIP mechanism significantly increases the work hardening rate and postpones the failing at the necking area, which results in higher strain levels than normal plastic deformation without involving the TRIP effect (see Figure 7).

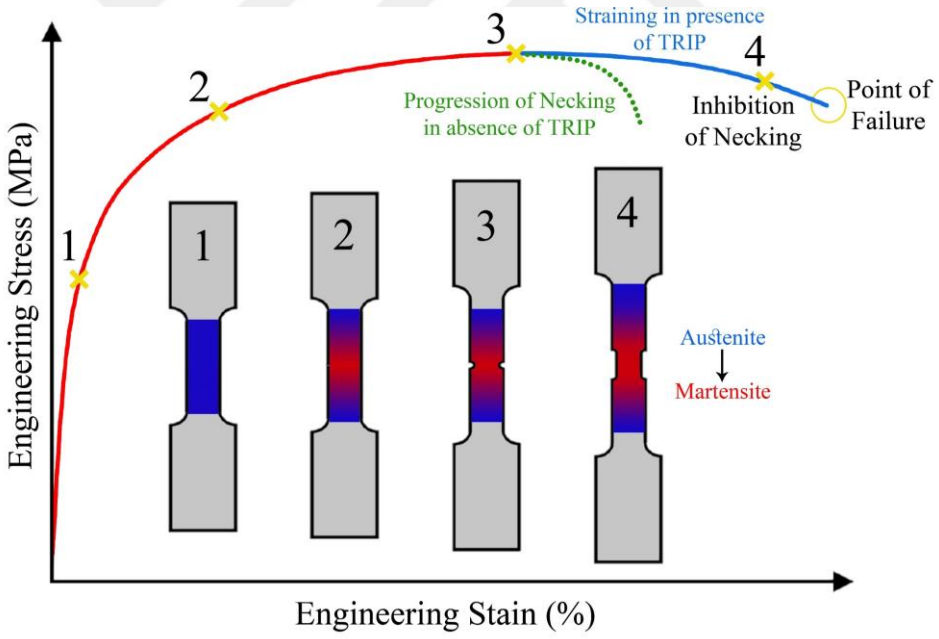

Stage 1: Elastic region (no dislocation movements)
Stage 2: Plastic region (dislocation movements & TRIP initiation)
Stage 3: Plastic region (dislocation movements & necking initiation & slight TRIP)
Stage 4: Plastic region (dislocation movements & necking & fully TRIP)

Figure 7. Schematic representing different stages during elastic and plastic regions and TRIP mechanism involved stages.

The main key to a superior strength-ductility synergy is intensifying the strain hardening ability to carry on with flow stress and postpone the plastic instability during plastic deformation. The phase transformation mechanism is an influential factor that can improve the strain hardening capability during plastic deformation. Throughout the transformation-induced plasticity (TRIP), the base austenite as the soft domain (FCC) transforms to the martensite as the hard domain (BCC) [76]. In TRIP-base designs, the strategy is designing and fabricating a low stacking fault energy (SFE) alloy system to stimulate the TRIP and twinning induced plasticity (TWIP) mechanisms in the microstructure. In the plastic deformation process of a low SFE system, the whole dislocation intercepts into Shockley particle dislocation [77,78], and leads to the generation of stacking faults (SFs) and deformation twins (DTs) as deformation substrates. These mechanisms by developing deformation substrates enhance the strength-ductility synergy.

Plastic deformation starts with dislocation movements and carries on by the introduction of dislocation pileups in the grains. Ou et al. have reported that under the TRIP mechanism, dislocations in the soft domain (FCC) are consumed profoundly by creating the hard domain (BCC) in the microstructure [79]. Therefore, a metastable MPEA with the presence of a TRIP mechanism can solve the strength-ductility trade-off besides opening vast research areas containing various design abilities to find superior characteristics in MPEAs.

2.7 Effect of Elements in TRIP Mechanism

Different elements can have different effects on the phases' amounts and their atomic crystal structures. When we talk about the effects of elements on the TRIP mechanism, the effects of elements on stabilizing the austenite phase should also be discussed. Carbon (C) is one of the components that can stabilize the austenite phase in the microstructure. It has been

proved that the carbon amount in the system should be limited to 0.3 wt% [80]. Moreover, Manganese (Mn) is another element that can help the TRIP mechanism with stabilizing the austenite phase in the alloy system. Adding Mn in the MPEA alloys has been reported up to 35 wt% [81]. However, other elements can limit the austenite phase in the alloy system. Aluminum (Al) and Silicon (Si) are two elements that destabilize the austenite and prevent the TRIP effect [82,83].

2.8 Annealing Twins

Twinning is known as a pair of separate grains that contribute to a crystal lattice in a symmetrical approach so that the atomic arrangement in grain A can be produced from grain B by reflection across a common plane (see Figure 8). In twins, the atomic crystal structure in both grains is the same, but the difference is in various orientations in space. For instance, the atomic sequence in {111} FCC planes as parent grains can produce twins by 60° rotation to <111> direction (see Figure 8). Annealing twins can be introduced in different materials such as simple alloy systems to advanced alloy systems like MPEAs [84].

The annealing twins happen in recrystallization processes and grain growth, and they occur mostly in FCC crystal structure which possesses low to medium stacking fault energy. Annealing twins were reported by Carpenter and Tamura for the first time in 1926. These crystal structures happen because of growth interceptions during recrystallization processes that apply on deformed cubic close-packed (here means FCC atomic crystal structure). In the twinning process, the stacking sequence of FCC crystal is changed from ABCABCABC… to ABCABACBA… at {111} planes. The annealing twins due to their atomic crystal structure have low interfacial energy at their grain boundaries [85].

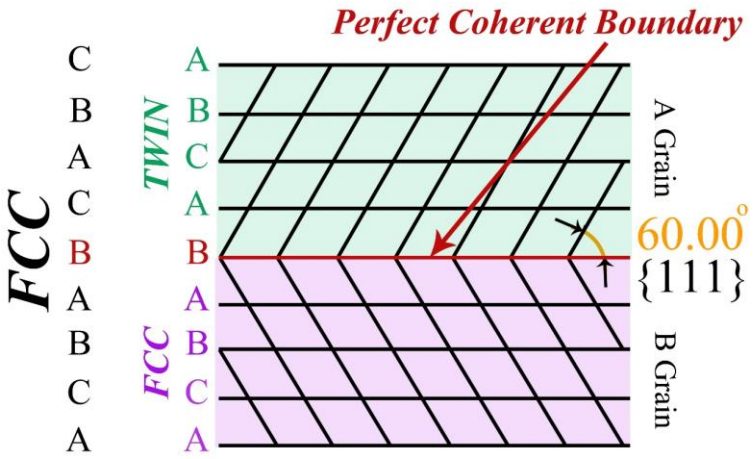

Figure 8. Schematic representing the twin structure and its sequence in an FCC atomic crystal structure.

These twins' generation depends on multiple parameters like grain size, presence of inclusions, level of applied plastic deformation, crystallographic specifics, present stacking fault energy, grain boundary energy, annealing time, and applied annealing temperature. In the annealing process, the twin continues to grow up until another growth incident happens, then the FCC atomic crystal stacking sequence inverted again and continue in the normal stacking sequence [86].

…ABCABACBA…CBACBCABC…

In the mentioned atomic sequence layers, layer B (represented by red color) shows the twin interfaces. For a coherent twin boundary, boundary planes are parallel to {111} planes, however, in incoherent twin boundary, the boundary planes are different than {111} planes. Annealing twin is an important process that regularly happens during the annealing process due to abundant grain boundaries' migration and their incident. The presence of annealing twins can alter the corrosion behavior and mechanical behaviors like fatigue life [87]. That is why studying this process in annealed samples is highly important.

2.9 Empirical Parameters: Valance Electron Concentration (VEC)

The empirical parameters were suggested based on Hume-Rothery rules [88] and the thermodynamic model of Takeuchi and Inoue [89]. This approach is representing that the stability in a solid solution is controlled by various factors. The atomic size difference, the electron concentration, and the difference in electronegativity are the parameters that determine the stability of a phase in a system.

Here, it has been tried to represent a meaningful and clear definition between thermodynamic matters and dependent characteristics in the design and fabrication of Multi-Element Alloys (High- and Medium Entropy Alloys) with focusing on the VEC values. In one sentence the stability of FCC and BCC solid solutions is well defined by the VEC amount. In the design and fabrication of alloys always stability of the present phase or phases is determinative, which eventually leads to the final mechanical behavior of the designed alloy. Therefore, having a proper comprehension of phase stability depending on the present atoms in such alloys is highly appreciated.

In general, the Multi-Principal Element alloys mostly employed Cu, Al, Ni, as FCC-based elements, Fe, Cr, Mo, and V as BCC-based elements, and Ti, Co as HCP-based elements in their atomic structure. It should be mentioned that a structure with a fully FCC atomic structure can be altered to FCC+BCC atomic structure and finally fully revolutionized to a BCC atomic structure just by altering the present elements. Obviously, shifting from an FCC to a BCC structure the mechanical properties of the alloy can transform from ductile to brittle behavior.

Replacing a specific element (assume element "A") in an alloy compound with another element (assume element "X"), with an atomic radius of more than the previous ones $R_X > R_A$ leads to lattice distortion energy (Figure 9). In such a situation, the system will try to decrease this distortion energy by forming a structure possessing a lower atomic-packing-efficiency structure which is known as BCC structure. It is highly recommended that all these concepts be translated to quantitative mathematic form instead of qualitative form.

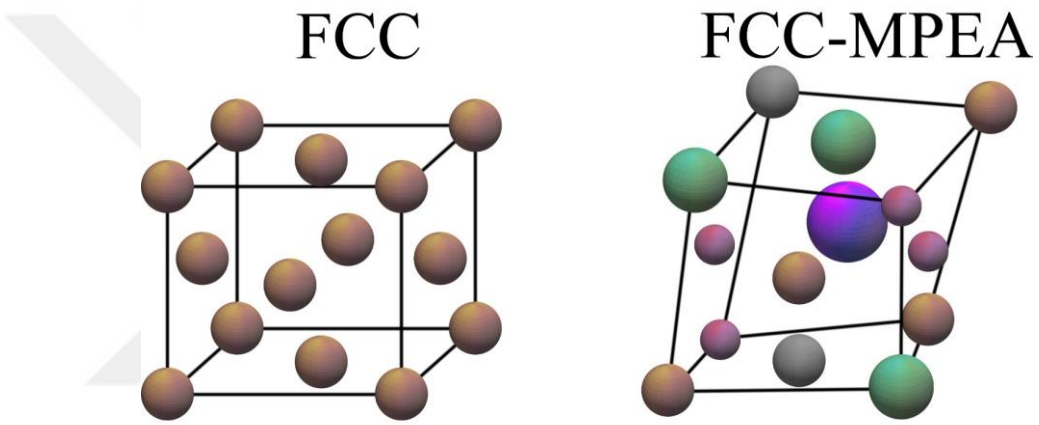

Figure 9. The schematic is illustrating the contribution effect of different atoms with different atomic radii on the distortion of the atomic crystal structure.

The atomic size difference (δ) can be illustrated as shown in equation 3. As an important point, it should be mentioned that $\delta < 6.6\%$ significantly increases the probability of one single-phase solid solution structure in the alloy [90].

$$\delta = 100 \sqrt{\sum_{i=1}^{N} c_i \left(1 - {}^{r_i}/_{\bar{r}}\right)^2} \qquad (3)$$

$$\bar{r} = \sum_{i=1}^{n} c_i r_i \tag{4}$$

While: c_i is the atomic percentage of the *i*th element, r_i is the atomic radius of the *i*th element

$$\Delta H_{mix} = \sum_{i=1, i\neq j}^{N} 4\Delta_{mix}^{AB} c_i c_j \tag{5}$$

where: Δ_{mix}^{AB} is the mixing enthalpy of binary liquid AB alloys

All mentioned equations are valid for multi-element alloys. Based on the present research the critical amount of ΔH_{mix} for forming a simple solid solution is: $-15\ kJ/mol \leq \Delta H_{mix} \leq 5\ kJ/mol$ and $1 \leq \delta \leq 6$. Furthermore, the boundary values of ΔS_{mix} for forming a simple solid solution will be [91]:

$$12\ J/K.mol \leq \Delta S_{mix} \leq 17.5\ J/K.mol$$

$$\Delta S_{mix} = -R \sum_{i=1}^{n} c_i \ln c_i \tag{6}$$

$$R\ is\ the\ gas\ constant, 8.314\ J/K.mol$$

Moreover, in the present system as long as $\Omega > 1.1$, the effect of the mixing entropy is greater than that of the enthalpy of mixing at the melting point, so high entropy phase(s) will tend to be formed [91].

$$\Omega = \frac{T_m \Delta S_{mix}}{|\Delta H_{mix}|} \tag{7}$$

In the further step, the melting temperature for the designed alloy can be calculated using:

$$T_m = \sum_{i=1}^{n} c_i (T_m)_i \tag{8}$$

Fang et al. [92] demonstrated that:

$$\Delta\chi = \sqrt{\sum_{i=1}^{n} c_i (\chi_i - \bar{\chi})^2} \tag{9}$$

$$\bar{\chi} = \sum_{i=1}^{n} c_i \chi_i \tag{10}$$

Where χ_i is the Pauling electronegativity for the *i*th element. Table 3 represents the most used elements in multi-principal element alloys with their electronegativity, atomic radius, and VEC amount. In the multi-principal element alloys the average number of itinerant electrons per atom (e/a), and the number of total electrons in the valence band (VEC) is the same. Therefore, the possible phases can be easily introduced according to the represented equation and introduced boundaries [93].

$$e/a \ or \ VEC = \sum_{i=1}^{n} c_i (e/a \ or \ VEC)_i \tag{11}$$

$$7.7 < VEC < 8.9 \ \ (FCC) \tag{12}$$

$$6.8 < VEC < 8.5 \ \ (FCC + BCC) \tag{13}$$

$$4.2 < VEC < 8.2 \ (BCC) \tag{14}$$

Table 3. Elemental data

Element	*Atomic Number*	*Electrons Configuration*	*Atom Radii (pm)*	*Pauling Electronegativity*	*VEC*	*T_m (℃)*
B	5	$[He]2s^2 2p^1$	87	2.04	3	2075
C	6	$[He]2s^2 2p^2$	67	2.55	4	3550
N	7	$[He]2s^2 2p^3$	56	3.04	5	-210
Al	13	$[Ne]3s^2 3p^1$	118	1.61	3	660
Si	14	$[Ne]3s^2 3p^2$	111	1.90	4	1414
Sc	21	$[Ar]4s^2 3d^1$	184	1.36	3	1541
Ti	22	$[Ar]4s^2 3d^2$	176	1.54	4	1668
V	23	$[Ar]4s^2 3d^3$	171	1.63	5	1910
Cr	24	$[Ar]4s^1 3d^5$	166	1.66	6	1907
Mn	25	$[Ar]4s^2 3d^5$	161	1.55	7	1246
Fe	26	$[Ar]4s^2 3d^6$	156	1.83	8	1538
Co	27	$[Ar]4s^2 3d^7$	152	1.88	9	1495
Ni	28	$[Ar]4s^2 3d^8$	149	1.91	10	1455
Cu	29	$[Ar]4s^1 3d^{10}$	145	1.90	11	1084
Ga	31	$[Ar]4s^2 3d^{10} 4p^1$	136	1.81	3	29
Zr	40	$[Kr]5s^2 4d^2$	206	1.33	4	1855
Nb	41	$[Kr]5s^1 4d^4$	198	1.60	5	2477
Mo	42	$[Kr]5s^1 4d^5$	190	2.16	6	2623
Ru	44	$[Kr]5s^1 4d^7$	178	2.20	8	2334
Rh	45	$[Kr]5s^1 4d^8$	173	2.28	9	1964
Pd	46	$[Kr]4d^{10}$	169	2.20	10	1555
Sn	50	$[Kr]5s^2 4d^{10} 5p^2$	145	1.96	4	231
Hf	72	$[Xe]6s^2 4f^{14} 5d^2$	208	1.30	4	2233
Ta	73	$[Xe]6s^2 4f^{14} 5d^3$	200	1.50	5	3017
W	74	$[Xe]6s^2 4f^{14} 5d^4$	193	2.36	6	3422
Re	75	$[Xe]6s^2 4f^{14} 5d^5$	188	1.90	7	3186
Os	76	$[Xe]6s^2 4f^{14} 5d^6$	185	2.20	6	3033
Ir	77	$[Xe]6s^2 4f^{14} 5d^7$	180	2.20	6	2466
Pt	78	$[Xe]6s^1 4f^{14} 5d^9$	177	2.28	6	1768

CHAPTER III

EXPERIMENTAL METHODS

3.1 Selecting the composition and general design concept

Based on research works, it has been stated that the atomic size, electronegativity, average and standard deviation of the itinerant electron concentration, and atomic bonds mismatch parameters can change via fraction changes in the amounts of the elements. Altering in mentioned values can shift the dominant phase from FCC to BCC phase in the MPEAs and vice versa. The main factor in alloy design is the VEC value and is the only factor that responds accurately to any change in the atomic crystal structure of the present solid solution.

In heterogeneous MPEAs it is highly recommended to start the design with a single FCC and/or BCC atomic crystal structure with $VEC > 7.7$ and $VEC < 8.2$ for FCC and BCC phase structures respectively (see Figure 10) [94]. It means that, if it is targeted to have a main phase of BCC, it should be started with a composition with VEC values lower than 8.2. Then, the composition should be evolved by adding other elements and changing the VEC value to tune the microstructure and mechanical behavior.

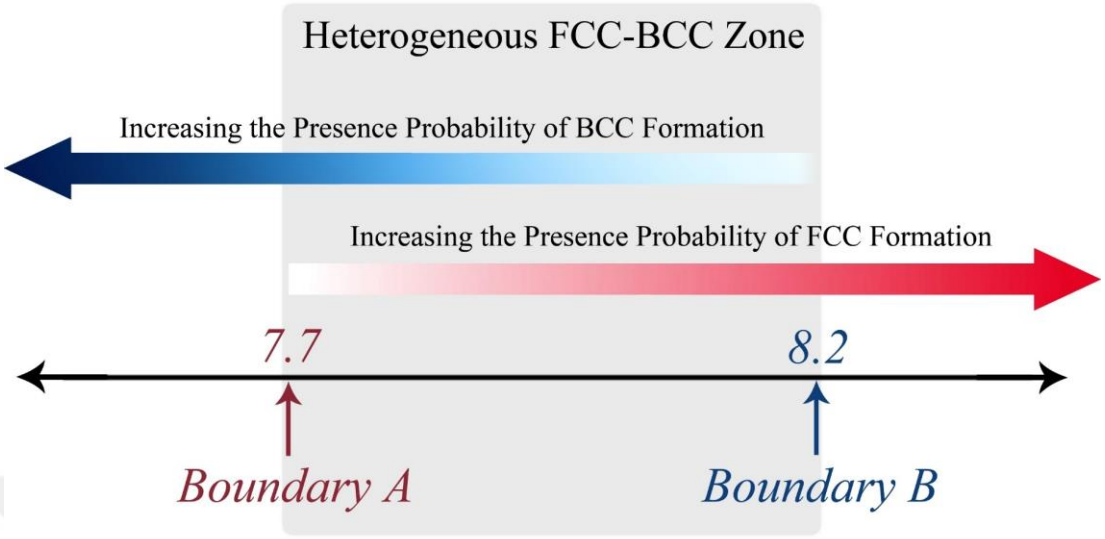

Figure 10. Schematic representing the boundary conditions for FCC, BCC, and FCC-BCC atomic crystal structures.

The atomic size difference can affect the distortion level of the atomic crystal structure, so tuning the mechanical behavior is easily accessible by altering the amounts of the atomic size difference. For instance, it is expected that the highest hardness and strength, and lowest ductility are obtained with a single BCC atomic crystal structure by shifting to the value of VEC to 6.13 [37].

Based on the literature review it has been decided to go with elements of Nickel (Ni), Chromium (Cr), Cobalt (Co), Iron (Fe), and Manganese (Mn) to stimulate the presence of FCC crystal structure in the alloy composition as the first composition. After multiple trials and errors, the alloy with a nominal composition of 25Ni-30Cr-30Fe-10Mn-5Co at% has been selected to carry on. For the second composition elements of Nickel (Ni), Iron (Fe), Cobalt (Co), Chromium (Cr), Titanium (Ti), and Molybdenum (Mo) to stimulate the mu (μ)-phase in an FCC-BCC heterogeneous MPEAs. The final nominal composition of 32Ni-25Fe-25Co-6Cr-6Ti-6Mo at% has been chosen for production and fabrication. These compositions

have been confirmed via two different approaches, theoretical and mathematical calculation, and thermodynamic calculations by employing simulation software.

3.1.1 The VEC calculations for 1st composition

$$= \sum_{i=1}^{5} C_i r_i = C_{Ni} r_{Ni} + C_{Cr} r_{Cr} + C_{Fe} r_{Fe} + C_{Mn} r_{Mn} + C_{Co} r_{Co}$$

$$\Longrightarrow \bar{r} = 157.55\ pm$$

$\therefore \delta$:

$$\delta = 100 \sqrt{\sum_{i=1}^{5} c_i (1 - {}^{r_i}/_{\bar{r}})^2}$$

$$= 100 \sqrt{\begin{matrix} C_{Ni}\left(1 - {}^{r_{Ni}}/_{\bar{r}}\right)^2 + C_{Cr}\left(1 - {}^{r_{Cr}}/_{\bar{r}}\right)^2 + C_{Fe}\left(1 - {}^{r_{Fe}}/_{\bar{r}}\right)^2 + C_{Mn}\left(1 - {}^{r_{Mn}}/_{\bar{r}}\right)^2 \\ + C_{Co}\left(1 - {}^{r_{Co}}/_{\bar{r}}\right)^2 \end{matrix}}$$

$$\Longrightarrow \delta = 4.1689\ \%$$

For having a proper MPEA, possessing a small difference in atomic radii δ of the present elements in the understudied alloy composition is vital. As mentioned previously this value should be less than 6.6%, which here is 4.1%. Thus, it seems that the proposed alloy composition is on a proper path to take the next steps.

$\therefore \Delta H_{mix}$:

Table 4. The values of Hmix (kJ/mol) calculated by Miedema's model for atomic pairs between elements for 1st composition [95].

Element	*Ni*	*Cr*	*Mn*	*Co*
Fe	-2	-1	0	-1
Ni		-7	-8	0
Cr			2	-4
Mn				-5

$$\Delta H_{mix} = \sum_{i=1, i\neq j}^{5} 4\,\Delta H_{AB}^{mix}\, c_i c_j$$

$$\Delta H_{mix} = -4.02\ kJ/mol$$

$\therefore \Delta S_{mix}$:

$$= -R \sum_{i=1}^{5} c_i \ln c_i$$

$$= -R\{C_{Ni} \ln C_{Ni} + C_{Cr} \ln C_{Cr} + C_{Fe} \ln C_{Fe} + C_{Mn} \ln C_{Mn} + C_{Co} \ln C_{Co}\}$$

$$\Longrightarrow \Delta S_{mix} = 1.44\ R\ or\ 11.978\ J/K.mol$$

ΔS_{mix} value reveals that the present condition for having a single-phase structure is proper.

$\therefore VEC$:

$$= \sum_{i=1}^{5} C_i (VEC)_i$$

$$= C_{Ni}(VEC)_{Ni} + C_{Cr}(VEC)_{Cr} + C_{Fe}(VEC)_{Fe} + C_{Mn}(VEC)_{Mn}$$

$$+ C_{Co}(VEC)_{Co} =$$

$$\Longrightarrow VEC = 7.85$$

So, we will have an FCC+BCC structure for the present alloy.

$\therefore \bar{\chi}$:

$$\bar{\chi} = \sum_{i=1}^{5} c_i \chi_i = C_{Ni}\chi_{Ni} + C_{Cr}\chi_{Cr} + C_{Fe}\chi_{Fe} + C_{Mn}\chi_{Mn} + C_{Co}\chi_{Co}$$

$$\Longrightarrow \bar{\chi} = 1.7735$$

$\therefore T_m$:

$$= \sum_{i=1}^{5} c_i (T_m)_i = C_{Ni}(T_m)_{Ni} + C_{Cr}(T_m)_{Cr} + C_{Fe}(T_m)_{Fe} + C_{Mn}(T_m)_{Mn} + C_{Co}(T_m)_{Co}$$

$$T_m = 1596.6\ ℃$$

Using ThermoCalc for different temperatures the present phases have been calculated. This work enables us to have a vision of the selected thermomechanical processes that want to be applied to the samples. For example, here the present phases with their detailed information reported for 900 ℃. There are two phases as FCC and BCC (calculated via ThermoCalc):

30Fe-27Ni-26Cr-10Mn -5.4Co (FCC-structure)

58Cr-23Fe-8Mn-7Ni-3Co (BCC-structure)

The results are showing that the alloy possesses a dominant ductile FCC structure and a less ductile high chromium (Cr) phase with a BCC crystal structure.

$$(VEC)_{FCC} = 0.3(8) + 0.27(10) + 0.26(6) + 0.1(7) + 0.054(9) = 7.846$$

$$(VEC)_{BCC} = 0.58(6) + 0.23(8) + 0.08(7) + 0.07(10) + 0.03(9) = 6.85$$

Here the values of 7.846 and 6.85 have been acquired for the hypothetical phases of FCC and BCC, respectively. As mentioned, a high VEC is contributing to forming FCC phase that delivers enhanced ductility, however, a low VEC is constructive in forming BCC phase with superior strength. Selecting ideal elements, based on the VEC, is a practical method for the design and fabrication of MPEA compositions that balance strength and ductility.

According to the calculations in detail, the 25Ni-30Cr-30Fe-10Mn-5Co at% is decided to take to further steps due to:

i. High potential of ductility.
ii. High potential of causing a single phase of FCC at higher temperature and a heterogeneous microstructure via introducing an FCC-BCC combination in the alloy.
iii. High potential of providing acceptable YS and UTS values.

3.1.2 Thermodynamical Based Simulation

The chosen composition after numerous reviews and calculations was run by two different thermodynamic base software. The employed software was using the CALPHAD method for their calculation. The CALPHAD method is a trustable way to approach as long as reliable thermodynamic databases are available for the software. Going through such a process help to make better decisions about our products and boost the materials design and fabrication process circumstances more accurately and reliably.

Figure 11 is representing the ThermoCalc simulated phase diagram for the understudied composition. According to the presented phase diagram, it can be understood

that the alloy microstructure is a single phase at higher temperatures (1080 ℃ up to the melting point). This characteristic is vital for applying the homogenization step since for a complete homogenized structure having just one single phase is highly appreciated. By advancing to lower temperature the phase diagram is showing a double phase structure of FCC-BCC and is proving that with decreasing the temperature the BCC phase is getting favorable thermodynamically. The acquired data is showing that the BCC phase cannot be produced more than 10% through thermomechanical processes.

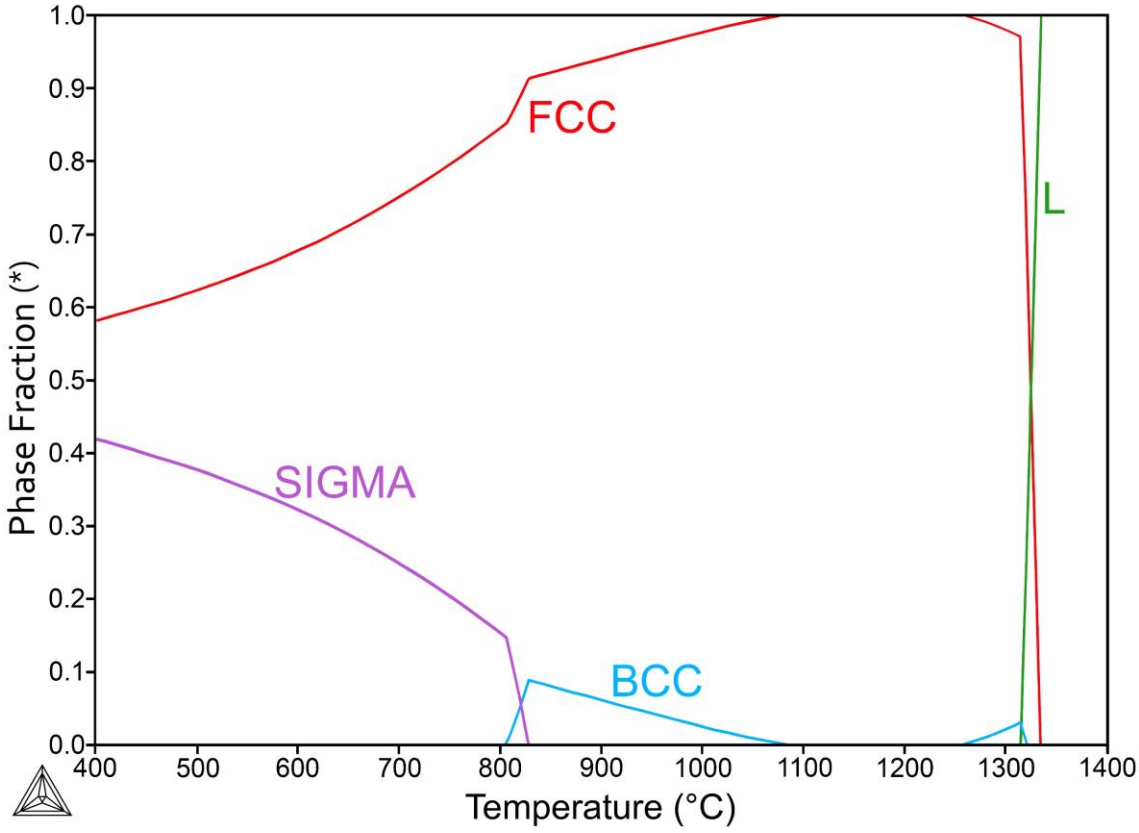

Figure 11. Calculated phase diagram for the 25Ni-30Cr-30Fe-10Mn-5Co at% at the ThermoCalc thermodynamic software.

The phase diagram is demonstrating that after passing 825 ℃ to a lower temperature the third phase known as the sigma phase produces and the amount of this phase is increasing

constantly with decreasing temperature. It seems that the presence of the Cr-rich sigma phase is more favorable thermodynamically in comparison to BCC, ever since the BCC phase is eliminated from alloy microstructure after 805 ℃.

The acquired results from thermodynamic software are not trustable and accurate. There is a possibility that some phases are introduced in the microstructure at slightly different temperatures. In addition, the contribution of the anticipated phase in software at a specific temperature can be different in experimental outcomes. This software just provides a general view of what should be expected from the designed alloy before taking any advanced step.

3.2 Heat treatment details for 1st composition

3.2.1 Selecting Post-annealing Temperature

As shown in Figure 11, the alloy melts around 1350 ℃ which is 246.6 ℃ lower than the value calculated based on the atomic characteristics. The difference between the actual melting temperature and the calculated temperature can be referred into two main reasons: the macro-level point of view, such as the accuracy of detectors and the environmental conditions, and the atomic level point of view, like assuming a perfect atomic crystal structure. Figure 11 is representing that by proceeding from melting point to lower temperatures the microstructure evolves to double FCC-BCC phase from a single FCC phase structure and then a triple FCC-BCC-Sigma -structure. Thermodynamically the alloy system prefers to develop a multi-phase microstructure with decreasing working temperature because of decreasing $-T\Delta S_{mix}$ contribution in Gibbs free energy.

Conceptually the homogenization process should develop a single-phase in the microstructure. The motivation in this step is causing grains with the least deviation in size and distribution. The calculated phase diagram for the alloy is representing a single-phase structure at 1080 ℃ to 1380 ℃, so the homogenization temperature should be chosen in this temperature range. For this process, 1150 ℃ was chosen for the homogenization temperature because of having a trustable distance from the edge temperatures of 1080 ℃ and 1380 ℃ since the software always can have errors.

This alloy has been designed and fabricated for the first time. Therefore, the alloy should be tested at a high temperature before running any further fabrication methods. For this step, it is conventional to test the alloy in little mass in cube form with very sharp edges.

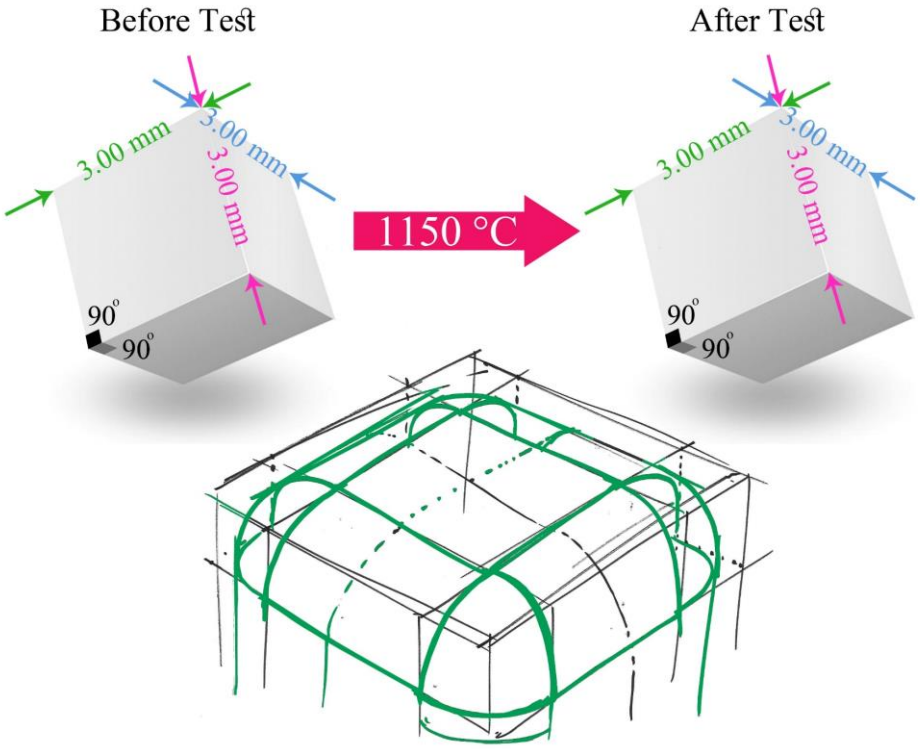

Figure 12. Schematic of the pre-step cube for understanding the thermomechanical behavior.

After the test, the edges supposed to be in perfect form with previous sharpness, length, and edge angle. During this test, a cube with 3×3×3 mm was prepared and tested for temperature behavior (see Figure 12). The alloy passed this test in perfect condition.

A double phase of FCC-BCC will help to develop a heterogeneous microstructure (different mechanical behavior). Therefore, three different temperatures of 750 ℃, 800 ℃, and 850 ℃ were selected to find and introduce a proper heterogeneous microstructure.

3.2.2 Selecting Post-annealing Duration

The post-annealing time is an important factor that determines the characteristics and quantity of the introduced phases in the microstructure. It can influence the amount of the annealing level which can affect the mechanical behavior in the fabricated alloy, therefore, the time parameter is very important to be considered. Hardness tests were performed on the cold-rolled alloy after post-annealing on the samples with dimensions of 3×3×1 mm for 15 min and 60 min.

Figure 13 is showing that longer annealing time leads to lower hardness and then lower mechanical behaviors. It seems that fully recrystallized microstructure is the reason, however, the 15 min is not enough for a full recrystallization process. Due to acquired results taking an average amount looks more suitable to get the optimum mechanical behavior, so a 30 min annealing duration was selected to proceed (see Figure 13).

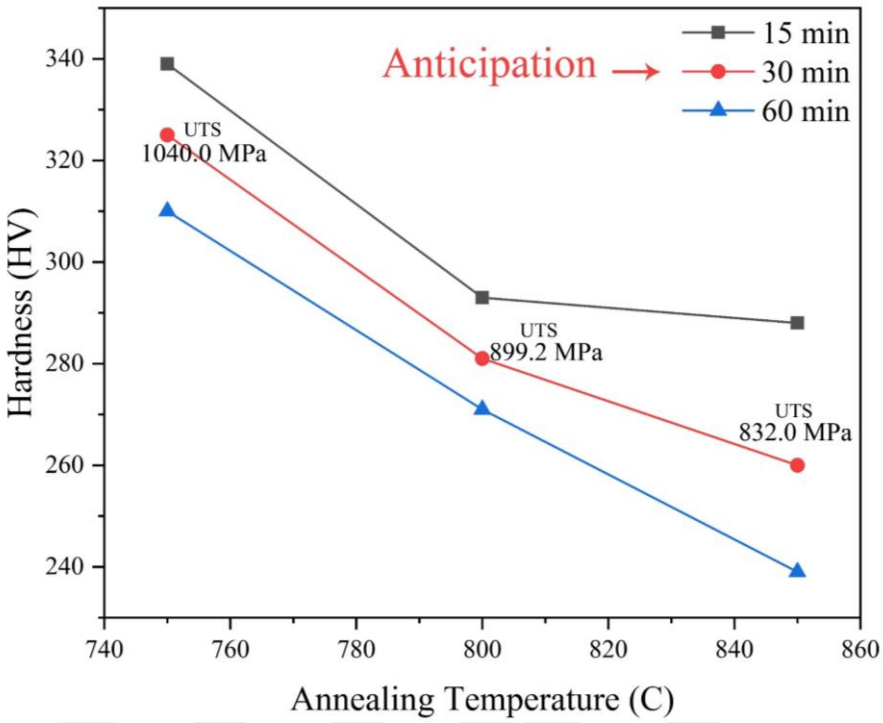

Figure 13. Microhardness results for post-roll annealing at 750 ℃ for 60 minutes (blue), 30 minutes (red), 15 minutes (black).

3.3 Thermo-mechanical processing for 1st composition

3.3.1 Vacuum Induction Melting (VIM)

The $Fe_{30}Cr_{30}Ni_{25}Mn_{10}Co_5$ (in at%) HEA after thermodynamical calculation approvements were cast via vacuum induction melting under an argon atmosphere (see Figure 14). Heating is done by an electric current that runs in a set of induction coils. The flowing of electrical current in the copper tube produces a magnetic field and goes through the crucible. Raw materials in the interaction of magnetic fields get melted and mixed. After being certain about the melting the homogenized melted composition runs to the Iron-mold (Figure 14a and b) via centrifuge force and fills it.

It is highly important to know the materials' heat radiation behavior, which is known as emissivity coefficient (ε). This coefficient contains amounts between 0 to 1 since 1 refers to an ideal black body. Employing an under-control atmosphere during the casting process eliminates oxygen and nitrogen from the casted ingot. Using VIM enables the composition to be very close to the nominal composition and gives an accurate casting (see Table 5).

Table 5. Nominal composition and cast ingot composition.

Element	*Target Composition at%*	*Casted Composition at%*
Fe	30	29.7
Ni	25	24.6
Cr	30	30.2
Mn	10	10.3
Co	5	5.2

Employing the VIM technique in comparison to other production methods enables the researcher to eliminate non-metallic additions and dissolved gasses. In addition, this approach decreases the macro-segregation to the least amount which can improve the mechanical behavior of the ingot. By decreasing the segregation of the melt during solidification needs for further steps to eliminate the segregation effect will fade out. In addition, the ability to work at a higher temperature under a vacuum circumstance provides a suitable situation for removing high vapored elements' gas pressure on and in the melt. Moreover, with access to higher working temperatures, the separation between non-metallic and high melting temperature unfavorable compounds with target composition becomes easier. In the case of microstructure, the VIM produces a system with fine diameter columnar for small size parts and equiaxed grains for larger ingots.

3.3.2 Homogenization

This step is running to introduce equiaxed grains with uniform FCC microstructure. The main goal in this step was to remove all phases except FCC atomic crystal structure from the alloy system. It is vital to have a uniform single phase to start other fabrication processes. Based on the calculated phase diagram, the FCC phase is the only present phase at a selected annealing temperature. As mentioned in the previous parts the MPEAs possess a highly distorted atomic crystal structure which enables these alloys to resist diffusion. So, the homogenization time should be long enough to let the system diffuse and thermodynamically reach the most stable form.

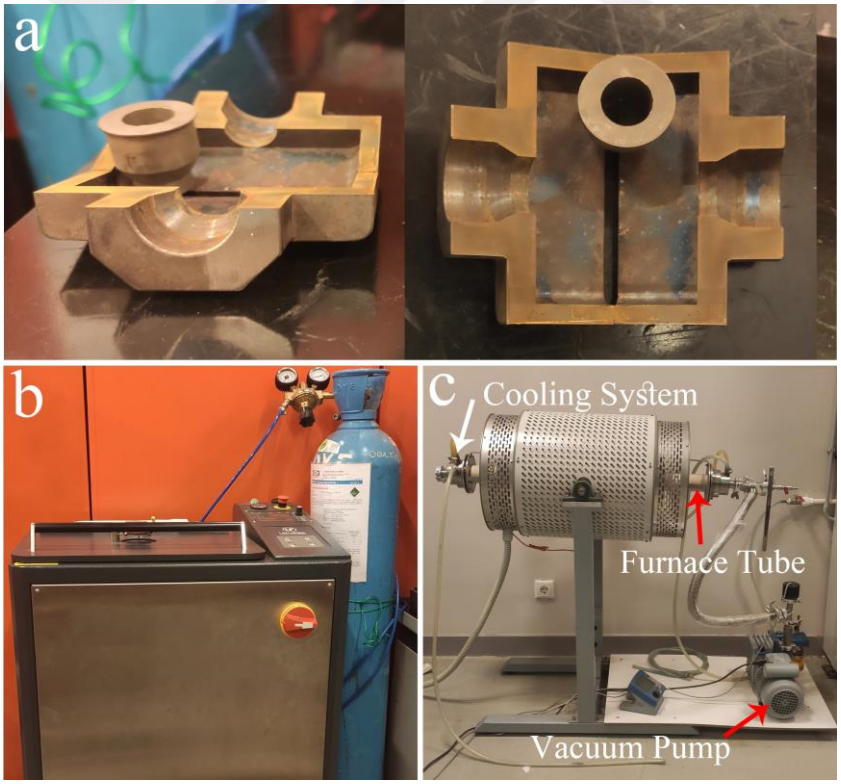

Figure 14. Casting and thermal process details (a) casting die's characteristics, (b) casting machine, (c) vacuum tube furnace.

The homogenization should be done at high temperature and long duration so protecting the samples was vital. Therefore, homogenization was carried out under a very controlled condition. A vacuum furnace was selected for this target. The ingots were homogenized at 1150 ℃ for 10 h in a vacuum furnace (see Figure 14c). During the whole process, the vacuum was about 7.2×10^{-2} mbar. After homogenization, all surfaces were machined 1mm in depth to remove every possible unfavorable compound such as oxides to make it suitable for the next step.

3.3.3 Plastic Deformation

Cold rolling is one of the main procedures in introducing submicron and nano-microstructure in the alloy system. This process is applied under the recrystallization temperature and most of the time is a combination of multiple steps of rolling to reach the final thickness (specific level of reduction). Rolling applied the plastic deformation in two dimensions (2D) and can cause material failure during the reduction process, and it is limited to the applied plastic level.

During the rolling process the material moves slower than the roll's speed (see Figure 15 part Ω_1) and after passing the rolls the material moves faster than the speed of rolls (see Figure 15 part Ω_3). Between these areas it is a neutral area with the speed of rolls speed, this zone is known as the neutral point (see Figure 15 part Ω_2). Before the neutral point, the friction force tends to drag the under-process material into the roll gap, since the material moves slower before the neutral zone. The neutral zone's position is determined by the adjustment of materials entrance speed with respect to the applied external force by the rolls. Therefore, the neutral zone does not have a specific area and it can alter based on the present circumstances in the process. As mentioned, the material is dragged into the rolls with present

friction in the process. Therefore, there should be a critical value for friction between the rolls and material to be able to run the cold rolling process.

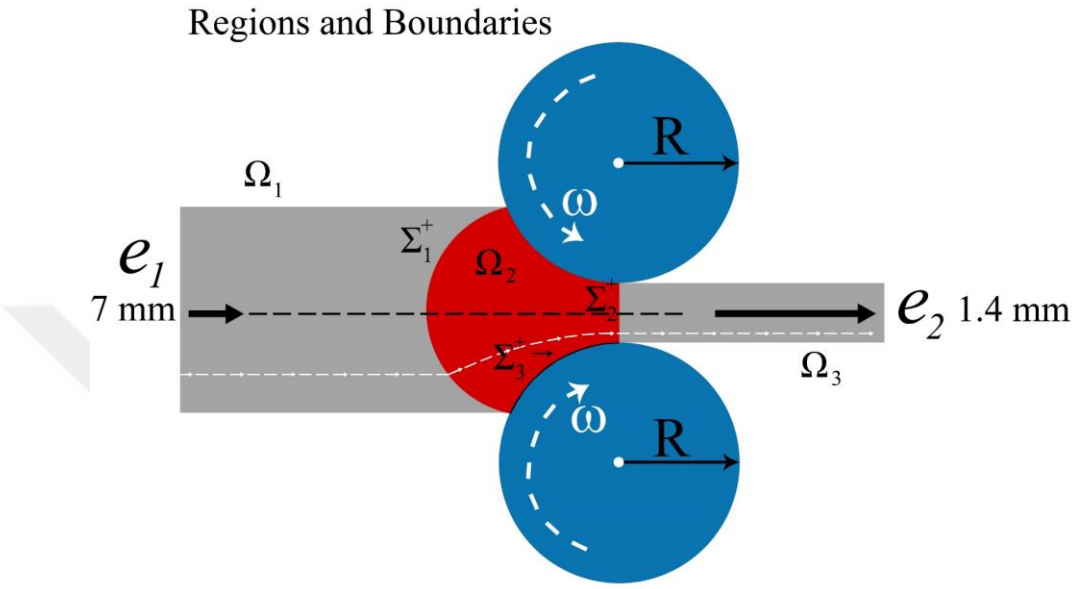

Figure 15. Schematic representing the rolling process and its related parameters and characteristics.

e_1	*Material thickness before rolling*
e_2	*Material thickness after rolling*
R	*Radii of roles*
w	*Roles' speed*
Ω_1	*MPEA Billet before rolling*
Ω_2	*Forming region or roll gap*
Ω_3	*MPEA Billet after rolling*
Σ_1^+	*The entrance of the roll gap*
Σ_2^+	*The exit of the roll gap*
Σ_3^+	*Arcs of contact between rolls and strip*

Figure 15 is representing the specifics of the rolling process in detail. The gray areas are showing the MPEA alloy, and the blue areas are illustrating the rolls employed in the system. During rolling the red part gets under plastic deformation and the curved can get more in Ω1 part and/or retreat based on characteristics of the rolled MPEA. The amount of plastic deformation is determining the microstructure characteristics so knowing the reduction level is important in the alloy fabrication procedure. The applied reduction level can be calculated with the following equation (eq. 15):

$$r = \frac{e_1 - e_2}{e_1} = 1 - \left(\frac{e_2}{e_1}\right) \rightarrow \frac{e_1}{e_2} = \frac{1}{1 - r} \tag{15}$$

The homogenized ingots were cut in 34×7×7 mm billets via a wire cut machine. The billets were rolled in multiple passes (each step 0.2 mm reduction) up to 1.4 mm thickness.

$$r = \frac{e_1 - e_2}{e_1} = \frac{7\ mm - 1.4\ mm}{7\ mm} = \frac{5.6\ mm}{7\ mm} = 0.8 \rightarrow 80\%$$

During the rolling process, the sample heated up to 73 ℃ which initiate from the applied huge plastic deformation on the atomic crystal of the material. After an 80% reduction on the billets, some cracks appeared at the edge part of the sheet which was smaller than 1.5 mm in most of the rolled billets.

3.3.4 Post-annealing processes

The slabs were sliced to dimensions of 34×7×7 mm, and then 80% reduction was applied by rolling at ambient temperature. Afterward, the fully homogenized and rolled billets were annealed for 30 minutes at three different annealing temperatures of 750 ℃, 800 ℃, and 850 ℃. Due to a lower temperature and shorter time in comparison to the

homogenization process a normal box furnace was employed in this step. The furnace left to stabilize at each annealing temperature for 30 min before putting the samples inside it. The samples were cooled down via quenching in water.

3.4 Theoretical Calculations for 2nd composition

3.4.1 The VEC calculations

$$= \sum_{i=1}^{6} C_i r_i = C_{Ni} r_{Ni} + C_{Fe} r_{Fe} + C_{Co} r_{Co} + C_{Cr} r_{Cr} + C_{Ti} r_{Ti} + C_{Mo} r_{Mo}$$

$$\Longrightarrow \bar{r} = 156.60\ pm$$

$\therefore \delta$:

$$\delta = 100 \sqrt{\sum_{i=1}^{6} c_i (1 - {}^{r_i}/_{\bar{r}})^2}$$

$$= 100 \sqrt{\begin{matrix} C_{Ni}\left(1 - {}^{r_{Ni}}/_{\bar{r}}\right)^2 + C_{Fe}\left(1 - {}^{r_{Fe}}/_{\bar{r}}\right)^2 + C_{Co}\left(1 - {}^{r_{Co}}/_{\bar{r}}\right)^2 + C_{Cr}\left(1 - {}^{r_{Cr}}/_{\bar{r}}\right)^2 + C_{Ti}\left(1 - {}^{r_{Ti}}/_{\bar{r}}\right)^2 \\ + C_{Mo}\left(1 - {}^{r_{Mo}}/_{\bar{r}}\right)^2 \end{matrix}}$$

$$\Longrightarrow \delta = 6.9565\ \%$$

As mentioned previously this value should be less than 6.6%, which here is 6.9565%. Thus, it seems that the proposed alloy composition is on defined boundaries. But it decided to carry on because this parameter is not the only determining parameter.

$\therefore \Delta H_{mix}$:

$$\Delta H_{mix} = \sum_{i=1, i\neq j}^{6} 4\,\Delta H_{AB}^{mix}\, c_i c_j$$

$$\Delta H_{mix} = -7.694\ kJ/mol$$

Table 6. The values of Hmix (kJ/mol) calculated by miedema's model for atomic pairs between elements for 2nd composition [95].

Element	*Fe*	Co	*Cr*	*Ti*	*Mo*
Ni	-2	0	-7	-35	-7
Fe		-1	-1	-17	-2
Co			-4	-28	-5
Cr				-7	0
Ti					-4

$\therefore \Delta S_{mix}$:

$$= -R \sum_{i=1}^{6} c_i \ln c_i$$

$$= -R\{C_{Ni} \ln C_{Ni} + C_{Fe} \ln C_{Fe} + C_{Co} \ln C_{Co} + C_{Cr} \ln C_{Cr} + C_{Ti} \ln C_{Ti} + C_{Mo} \ln C_{Mo}\}$$

$$\Longrightarrow \Delta S_{mix} = 1.56\ R\ or\ 13.004\ J/K.mol$$

ΔS_{mix} value reveals that the present condition for having a single-phase structure is proper and the composition is high entropy alloy.

$\therefore VEC$:

$$= \sum_{i=1}^{6} C_i (VEC)_i$$

$$= C_{Ni}(VEC)_{Ni} + C_{Fe}(VEC)_{Fe} + C_{Co}(VEC)_{Co} + C_{Cr}(VEC)_{Cr} + C_{Ti}(VEC)_{Ti} + C_{Mo}(VEC)_{Mo}$$

$$\Longrightarrow VEC = 8.41$$

It seems that most probably the system will have an FCC crystal structure due to the VEC value. In addition, allegedly the alloy system will introduce the BCC crystal structure in the alloy system since the SFE value will get affected due to mu (μ)-phase (stimulated by Molybdenum) presence in the microstructure.

$\therefore \bar{\chi}$:

$$\bar{\chi} = \sum_{i=1}^{6} c_i \chi_i = C_{Ni}\chi_{Ni} + C_{Fe}\chi_{Fe} + C_{Co}\chi_{Co} + C_{Cr}\chi_{Cr} + C_{Ti}\chi_{Ti} + C_{Mo}\chi_{Mo}$$

$$\Longrightarrow \bar{\chi} = 1.8603$$

$\therefore T_m$:

$$= \sum_{i=1}^{6} c_i (T_m)_i = C_{Ni}(T_m)_{Ni} + C_{Fe}(T_m)_{Fe} + C_{Co}(T_m)_{Co} + C_{Cr}(T_m)_{Cr} + C_{Ti}(T_m)_{Ti}$$

$$+ C_{Mo}(T_m)_{Mo}$$

$$T_m = 1595.73\ ℃$$

In this alloy, it can be understood that the VEC value is not the only determining factor. Even with higher VEC in one case, it can be expected to see a different microstructure than what the mathematical calculations are representing by a slight difference. But these calculations are showing a sketch of reality in low detail.

According to the calculations in detail, the 32Ni-25Fe-25Co-6Cr-6Ti-6Mo at% is decided to take to further steps due to:

i. High potential of ductility.

ii. High potential of causing a single phase of FCC at higher temperature and a heterogeneous microstructure via introducing an FCC-BCC-mu (μ) combination in the alloy.

iii. Great potential to reach Giga Pascal YS and UTS with high ductility.

3.4.2 Thermodynamic Based Simulation in 2nd composition

Figure 16 is illustrating the ThermoCalc simulated phase diagram for the second composition. The represented data is confirming that the system has a single phase at a higher temperature (1094 ℃ up to the Melting point). This characteristic at a higher temperature makes this alloy system capable of running homogenization without producing extra phases in the alloy microstructure.

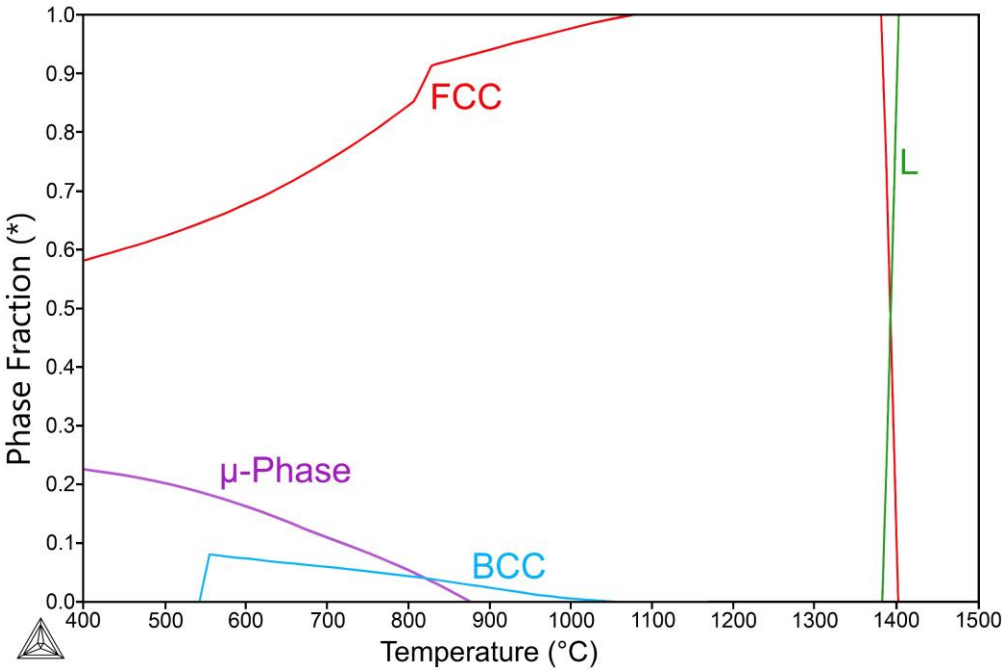

Figure 16. Calculated phase diagram for the 32Ni-25Fe-25Co-6Cr-6Ti-6Mo at% at the ThermoCalc thermodynamic software (due to sluggish diffusion rate at lower temperatures, the present phases at temperatures lower than 550 ℃ were eliminated from the calculated phase diagram).

Progressing to lower temperatures in the phase diagram introduces a heterogeneous microstructure of FCC+BCC in the alloy system. Moreover, by shifting to even lower temperatures the μ-phase as the third phase gets more favorable and an FCC+BCC+Mu phase combination is introduced in the alloy system.

This kind of alloy system is very suitable for employing both back- and forward-stress and pinning mechanisms (using μ-precipitation). The μ-phases can act as a proper barrier for locking the dislocations and strengthening the YS and UTS values. It seems that a combination of these mechanisms will significantly boost mechanical behavior.

3.5 Thermomechanical processing details for 2nd composition

After casting the alloy composition (Table 7), the billets were homogenized at 1150 ℃ (after high temperature cube test confirmation at 1150 ℃ for 10 h) for 10 h in a tube furnace under the vacuum condition of 7.2×10^{-2} mbar after confirmation of cube test (see Figure 12). The samples were quenched in water directly after the homogenization process. This attitude froze the atomic crystal structure in FCC form and was enable us to have a ductile base to carry on. Moreover, homogenization for 10 h introduced a courser grain structure that help to have more opportunity to apply 80% reduction on the billets with the least crack propagation at edges.

For decreasing wasted materials, the rolled billets were cut into multiple tensile samples before annealing aging processes. With a close look at the alloy phase diagram, it can be understood that for having an optimum combination of grain size, grain distribution, introducing BCC, introducing μ-phase, and their size and distribution a simple annealing plan will not include each single of them. Figure 16 is showing that the alloy is in the FCC+BCC

zone at 875-1094 ℃. This temperature range was selected to have annealing and introducing BCC phase and new grains and grain boundaries. Therefore, 900 ℃ was chosen as annealing temperature.

The samples were annealed at 900 ℃ for 5, 10, 15, 20, 25, and 30 minutes. These multiple annealing times were selected to have a general view on the effect of annealing at 900 ℃ and selecting the optimum annealing duration. Due to high oxidation possibility and losing the target chemical composition, the annealing processes were done under a controlled environment (tube furnace under 7.2×10^{-2} mbar vacuum). The samples were quenched in water to room temperature after each process.

Table 7. Nominal composition and cast ingot composition.

Element	*Target Composition at%*	*Casted Composition at%*
Ni	33	32.6
Fe	25	24.6
Co	25	25.4
Cr	6	6.3
Ti	6	6.1
Mo	6	6.0

The aging processes were applied to the annealed samples at 650 ℃. The calculated phase diagram (see Figure 16) is illustrating that the 541-875 ℃ temperature range is the best area to apply the aging step. A temperature lower than 600 ℃ is quite low for such distorted atomic crystal structure to have proper diffusion and introduce precipitates. On other hand, temperatures over 750 ℃ are high for having a long aging process. The 650 ℃ was selected for aging temperature which had all the above-mentioned boundary conditions and was far enough from boundary values in calculated boundary temperatures via ThermoCalc software. The aging processes were carried out for 180 minutes to introduce the desired microstructure.

3.6 Microstructural Characterization

3.6.1 X-ray diffraction analysis

X-ray diffraction is profoundly employed in characterizing the structure of the base materials at the atomic level. This method provides a general characterization of the whole material, and it is not specific to an exact region. So doing XRD studies can offer a general view of the present phases and their structures without missing information very easily. The phase characterization was conducted by employing X-Ray Diffraction (Bruker D8 Advance) with Cu-Kα radiation (wavelength 1.54056 Å) at a scanning range (2θ), step size, and time of 30º-100º, 0.02º, and 1s, respectively. Well-prepared polished flat surfaces were used for XRD analysis, doing so the samples were mechanically polished up to 2500 grit with SiC paper.

3.6.2 Scanning Electron Microscopy (SEM)

Scanning electron microscopy (SEM) is a microscopic approach where during scanning an electron beam radiates and an image is generated by gathering all signals backscattered from the surface of the sample. The emitted electrons and other participated radiation in image generation initiate from the primary electrons projected on the surface of the sample. The SEM equipped with energy-dispersive X-ray spectroscopy (EDS) detector was employed for fracture surface and elemental map analysis.

3.6.3 Electron backscatter diffraction (EBSD)

Electron backscatter diffraction (EBSD) analysis was performed using secondary and backscattered electrons. EBSD was carried out using field emission SEM (FEI XL30S) with a step size of 35 nm. The EBSD samples were prepared by mechanical polishing up to 1200

grit with SiC paper. These processes were followed by diamond paste (3 and 1 μm) and finished by colloidal silica polishing (0.4 μm). Results were analyzed via the orientation imaging microscopy (OIM) software (TSL OIM 7). The average grain sizes of the samples were acquired by employing high angle boundaries (HAGBs) without considering twin boundaries. Phase fractions were measured using EBSD results which were recorded from three different regions on the samples. Average values were reported, and the standard deviation of the phase fraction measurements was lower than 3%.

3.6.4 Transmission Electron Microscopy (TEM) analysis

For TEM studies specimens were cut by Struers Minitom low speed diamond saw. Thin foils were prepared by disc punching 3mm disks and grinding down to ~100μm. After that perforation was performed by electropolishing with an electrolyte of 20% perchloric acid + 80% ethanol solution at about –30 oC with 15V in Struers-Tenupol-5 Double Jet Electropolisher. Also, some electropolished specimens were further ion milled with Gatan 691 Precision Ion Polishing System (PIPS). Specimens were ion polished first at 4 kV for 1 hour, and then at final step at 2kV for 2hours.

The foils were examined with a JEOL JEM 2100 HRTEM operated at 200 kV. Images were taken by Gatan Model 794 Slow Scan CCD Camera and also by Gatan Model 833 Orius SC200D CCD Camera. Selected Area Electron Diffraction (SAED) and Energy Dispersive Spectrometry (EDS) techniques were used to investigate the microstructure. For digital images Gatan Microscopy Suite (GMS) 2 software was used. For EDS Oxford Instruments X-MaxN 80 T with Inca software system was used. For diffraction pattern analysis and crystallography purposes SingleCrystal and CrystalMaker softwares were used.

3.7 Mechanical Behavior Characterization

3.7.1 Vickers microhardness

Microhardness testing is an approach for measuring the materials' hardness with the least destruction with the capability of applying on a very small area (see Figure 17). Measuring the hardness of the materials can provide a general view of the behavior of the material with the least damage on the sample. The microhardness test can provide general information about the mechanical behavior of homogeneous and heterogeneous materials.

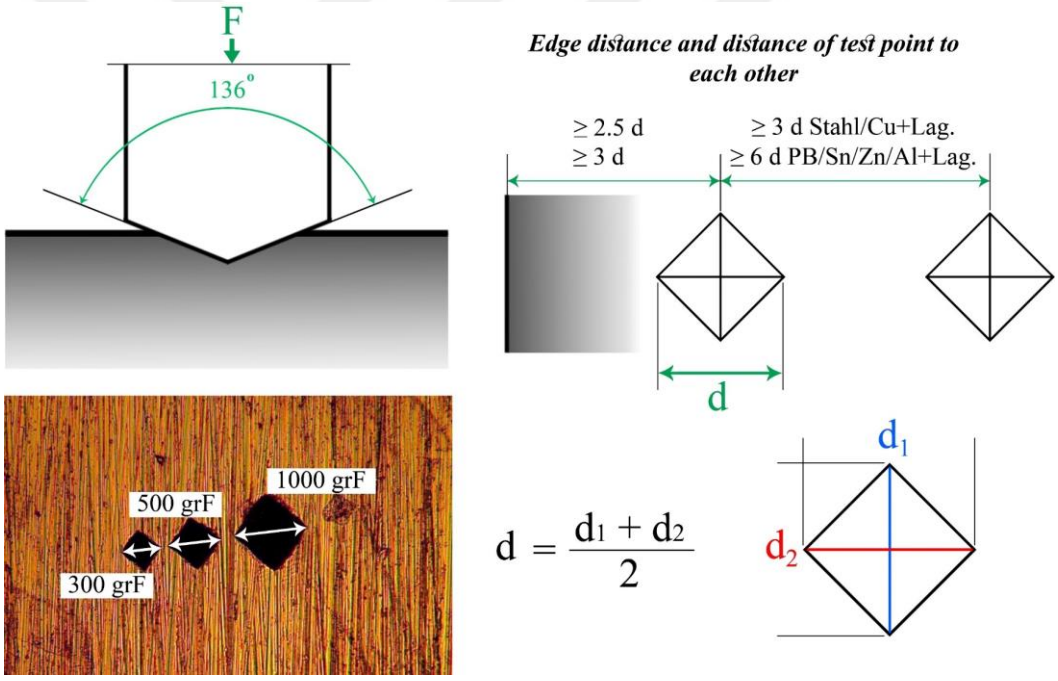

Figure 17. Schematic representing the Vickers microhardness test with related standards for avoiding wrong data and decreasing the errors.

In these tests, the Vickers microhardness measurements were performed with a load of 1000 gf for 15s to an indenter in a rhombus-shape (elongated four-sided pyramid). The 1000 gf was chosen based on the base hardness of the fabricated MPEA. Figure 17 is showing that how the base MPEA (the least hard condition) is reacting to different forces applied on

the surface of the samples. Due to increasing the hardness of the MPEA after the annealing process, having a proper d value for pyramid diagonal, and decreasing the error amounts the 1000 gf was selected for analysis. For eliminating the scratch effect on the results, the surface of the samples was well-polished up to 1200 grade sandpaper. The results for each condition were reported based on the average amounts of three hardness tests. The standard deviation of the reported values was determined to be lower than 5%. All the indentions were done away from the edge parts (based on mentioned standards in Figure 17) for eliminating edge effect error from all calculations.

3.7.2 Tensile studies

Tensile samples were prepared in a dog-bone shape (with a gage length, width, and thickness of 15, 3, and 1.4 mm, respectively) by employing electro-discharge machining (EDM) Figure 18. The samples were ground and polished to remove the adverse effects of scratches and residual layers. Uniaxial tensile tests were conducted on an Instron servo-hydraulic mechanical testing frame at room temperature with a strain rate of $10^{-3}\ s^{-1}$.

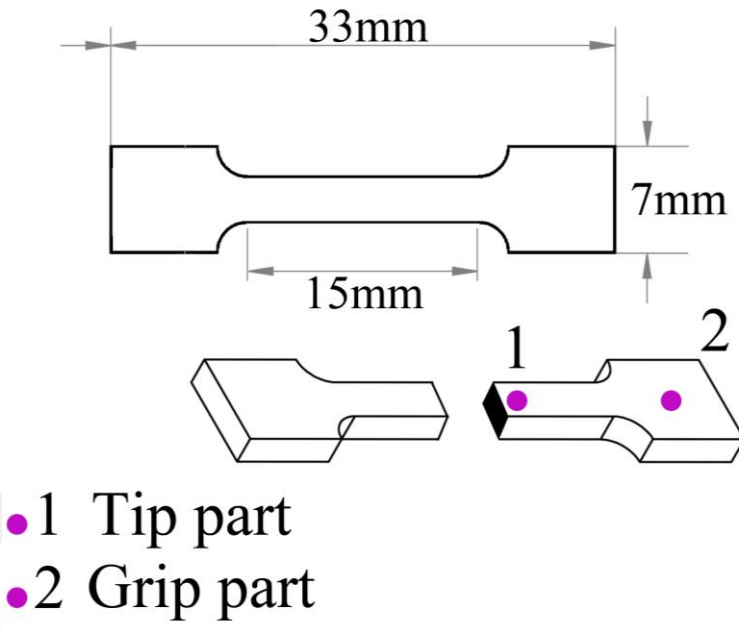

Figure 18. Schematic representing the characteristics of the dog-bone shape tensile sample, points 1 and 2 are illustrating the regions for EBSD characterization.

CHAPTER IV

RESULTS AND DISCUSSIONS

These sections are trying to represent all studies in-depth for 1st composition. The results for 2nd composition including only mechanical behavior studies are represented in the last section of this chapter.

4.1 Initial microstructures

The microstructural analysis of the as-received and rolled specimens is demonstrated in Figure 19. The XRD results show an FCC structure for both the as-received and rolled samples; however, after rolling, a strong (111) preferred crystal orientation was obtained in the microstructure of the rolled MPEA (see Figure 19 a-e). As shown in Figure 19d, the EBSD inverse pole figure (IPF) map of the as-received material represents equiaxed grains attributed to the homogenization process after casting.

The average grain size of the as-received material is about 159.1 μm with a standard deviation of 67.9 μm (see Figure 19d). On contrary, the IPF map of 80% rolled sample demonstrates ultra-fine grain (UFG) microstructures with a high density of grains with 111 atomic crystal orientation. Furthermore, non-uniform grain size distribution was detected after the rolling process (see Figure 19e).

By applying up to 80% thickness reduction via cold rolling, many dislocations are generated in the microstructure. These regions are represented by the black areas, which are not indexed by the EBSD detector, and could be related to shear bands with high accumulated strain (see Figure 19e). The Kernel average misorientation (KAM) maps can help for

providing the strain distribution regarding the dislocation density. The corresponding KAM value is calculated up to the third closest neighbor in the range of 0-5º for misorientation. With the calculation of KAM results, 0.337º and 1.688º values are determined for the as-received and rolled samples, respectively (see Figure 19f and g). The enhanced KAM value of the rolled sample indicates the presence of a high dislocation density microstructure. The presence of higher dislocation density can be translated to the ability in modifying the microstructure for further proper thermomechanical processes.

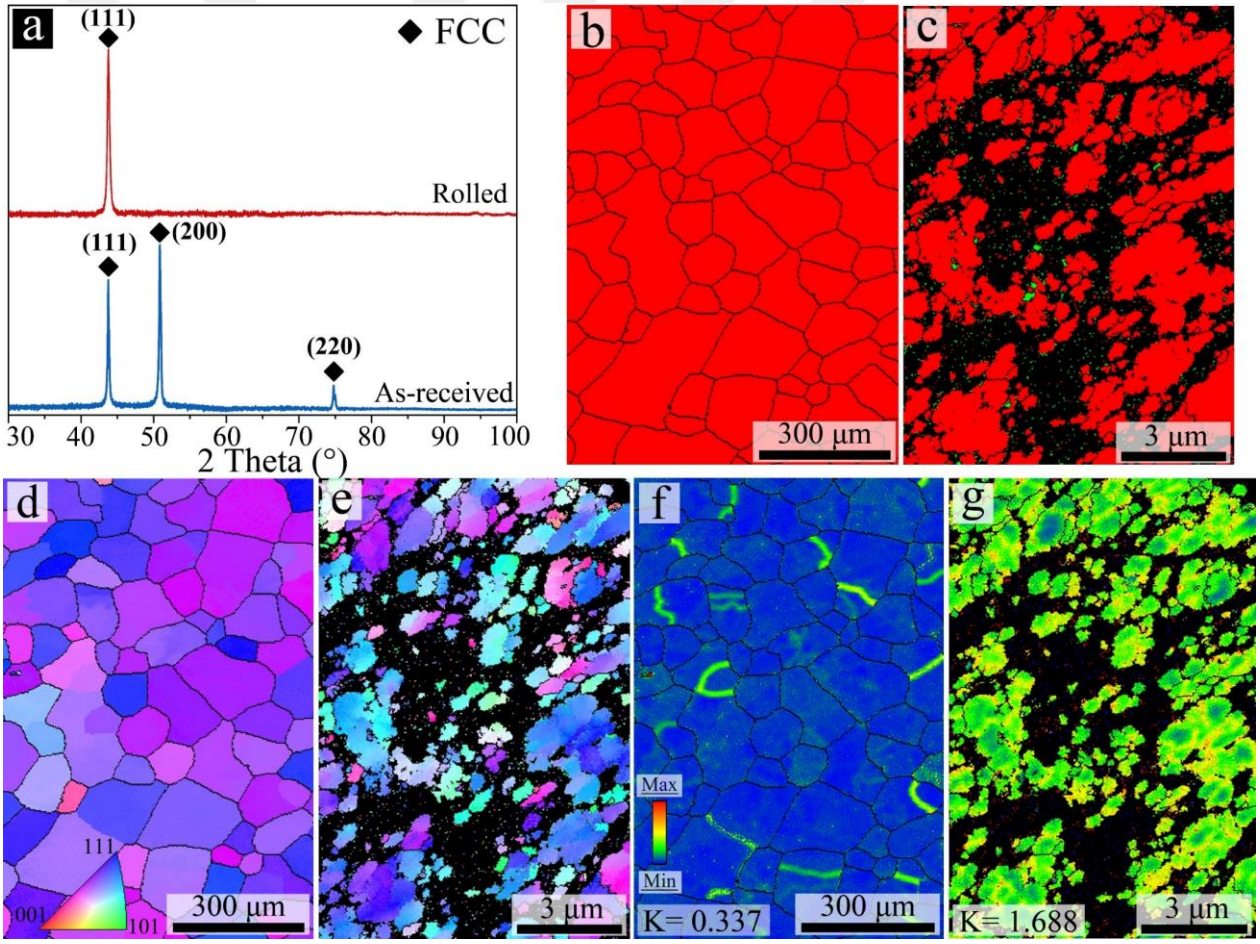

Figure 19. (a) The XRD patterns of as-received (blue) and 80% rolled (red) specimen, Phase map of (b) as-received and (c) rolled sample, EBSD inverse pole figure (IPF) map of (d) as-received sample and (e) rolled sample, Kernel average misorientation (KAM) maps of (f) as-received and (g) rolled samples.

Characterizing the homogenized samples by employing the EDS analysis was showed that the acquired composition after casting is close to the nominal composition Table 5. Therefore, the fabrication processes were carried based on the originally calculated phase diagram through the thermoCalc. Composition of target alloy and cast one.

4.2 Microstructural evolution during post-deformation annealing

4.2.1 XRD and EBSD analysis

The XRD results of the samples annealed at various temperatures are shown in Figure 20a. According to these results, the sample annealed at 750 °C consists of the dual-phase structure of FCC and BCC. As the annealing temperature increases to 800^{o}C, the structure changes from dual-phase to triple-phase, consisting of FCC, BCC, and Tetragonal atomic crystals. This holds for the 800^{o}C and 850^{o}C samples, where the tetragonal atomic crystal belongs to the sigma phases. The XRD results are corroborated by the microstructural changes observed by the EBSD characterizations (Figure 20b-f).

The post-deformation thermal treatments are performed at different temperatures of 750, 800, and 850 ℃ for 30 min to acquire the annealed microstructures with decent mechanical behavior. The presented EBSD micrographs in Figure 20b-f from the annealed samples are included in two different regions of the grip part (non-deformed region) and the tip part (deformed region close to the fracture taken from the uniform elongation area, not the necking part). It can be noticed that the microstructure of the sample annealed at 750 ℃ contains UFG microstructure with an average grain size of ~844 nm (Figure 20b).

Inspection of data from the phase map reveals a volume fraction of 94% for the FCC phase and 6% for the BCC phase, and no sigma phase is detected for the sample annealed at

750 ℃. However, the EBSD analysis at the tip part of the tensile specimen shows a higher BCC phase fraction of 18% (with 82% of FCC phase) as compared to the grip part (Figure 20c). The increase in the BCC phase fraction after tensile testing represents the occurrence of deformation-induced phase transformation during plastic deformation. In other words, the metastable FCC matrix transforms to the BCC martensite phase when loaded under tension, leading to an increase in the BCC-phase fraction by 12%.

The microstructure of the sample annealed at 850 ℃ (average grain size: ~1.3 μm) consists of a phase mixture with crystal structures of 86% FCC, 4% BCC, and 10% sigma phases at the grip part (Figure 20d). After tensile straining, the fraction of constituent phases is 82% FCC, 8% BCC, and 10% sigma phases at the tip part (Figure 20e), implying that FCC to BCC transformation also occurs in the 850 ℃ annealed sample. Also, Figure 20f presents the microstructure of the sample annealed at 800 ℃ where the fraction of constituent phases is 90% FCC, 5% BCC, and 5% sigma phase (at the grip part).

Accordingly, the sigma phase with tetragonal crystal structure appears after annealing at 800 ℃, where its fraction depends on the thermal driving force. Namely, the sigma phase fraction increases by elevation in the annealing temperature.

Careful evaluation of the XRD graphs and EBSD results (Figure 20) discloses the formation of a multi-phase heterogeneous microstructure (hard domain-soft domain) after post-rolling annealed conditions. In general, sigma phase formation highly depends on the parameters of thermo-mechanical processing, stoichiometry, and lattice defects [71,96,97].

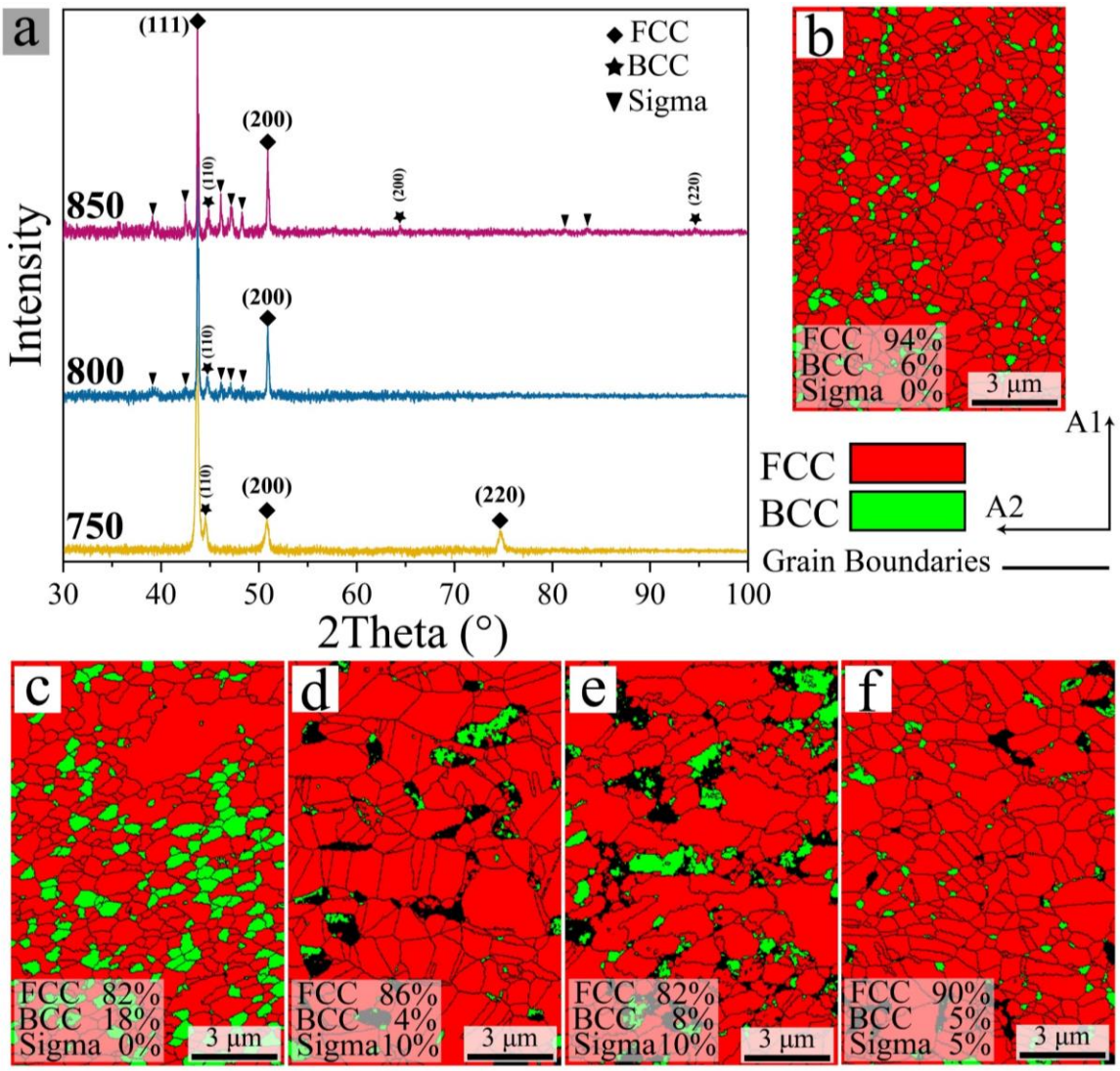

Figure 20. (a) The XRD patterns of the samples annealed at 750 ℃ (yellow), 800 ℃ (blue), and 850 ℃ (purple), EBSD phase maps of the samples annealed at (b) 750 ℃ taken from the grip part, (c) 750 ℃ taken from the tip part, (d) 850 ℃ taken from the grip part, (e) 850 ℃ taken from the tip part, and (f) 800 ℃ taken from the grip part.

It is reported that an increase in the annealing time and temperature stimulate the volume fraction of the Cr-rich phase (sigma) in the microstructure [73]. Based on the XRD graphs the sigma phase starts to introduce in the microstructure after 800 ℃. This phase is showing (002), (420), (222), and (430) planes at the highest annealing temperature. However,

due to the low available temperature at 800 ℃ the (430) plane is limited and other present planes at higher temperatures lose their intensity.

In addition, a significant amount of stored energy induced by severe plastic deformation can support the formation of sigma phase precipitates [38]. Based on the phase maps, it is concluded that a lower annealing temperature of 750 ℃ leads to almost no sigma phase in the microstructure, although this phase formation gets more favorable after annealing at higher temperatures. This confirms that there is a strong dependence of the microstructural evolution in this MPEA on the selection of processing parameters.

Comparing the phase distributions at the grip (non-deformed region) and the tip (deformed region) parts suggests a meaningful relation concerning the balanced formation of sigma and BCC phases. A lower volume fraction of the BCC phase with a less uniform distribution is provided with the introduction of a higher sigma phase fraction in the microstructure at higher annealing temperatures.

It appears that FCC to BCC transformation occurs in a limited manner for the samples annealed at and above 800 ℃. Moreover, sigma phase formation may be one of the main reasons that preclude reaching higher strain and stress levels simultaneously for these post-rolling annealed samples by limiting deformation-induced phase transformation and thus the potential benefit of TRIP effect [71,98].

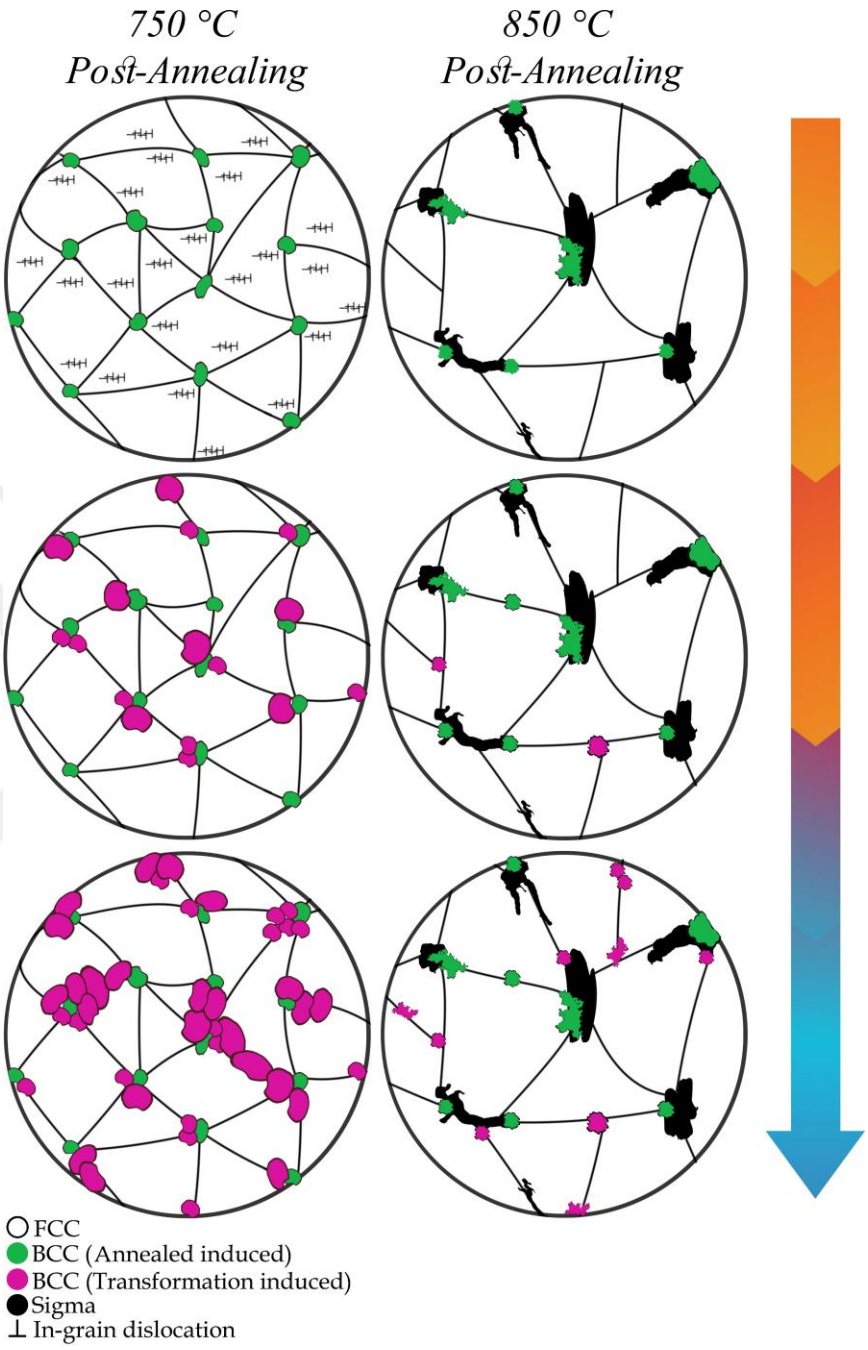

Figure 21. Schematic illustration of microstructural evolution in the rolled samples annealed at 750 ℃ and 850 ℃ during tensile deformation.

Microstructural heterogeneity is highly influential for dictating the trade-off behavior during plastic deformation in multiphase HEAs [99]. Heterogeneous distribution of hard

domains (BCC crystals) at grain boundaries of the soft domain, i.e., FCC matrix, profoundly stimulates the generation of localized deformation zones in the microstructure. With increasing grain size and decreasing homogeneity in phase distribution, the strain uniformity descends significantly, leading to lower YS and UTS at the higher annealing temperature of 850 ℃ [100]. Nevertheless, the 750 ℃ sample presents the near-optimum microstructure that provides the improved YS and UTS values besides a reasonable level of ductility.

4.2.2 Elemental Mapping

Figure 22 shows the SEM micrograph with corresponding EDS maps for the sample annealed at 850 °C. Phases, rich in Cr, are found inside the structure. These phases, marked by white arrows in Figure 22a also were observed in other research and are representing the sigma phases [96,101]. The SEM-EDS results are represented in qualitative form due to unsuccessful detection for determining the chemical composition of the present sigma phases.

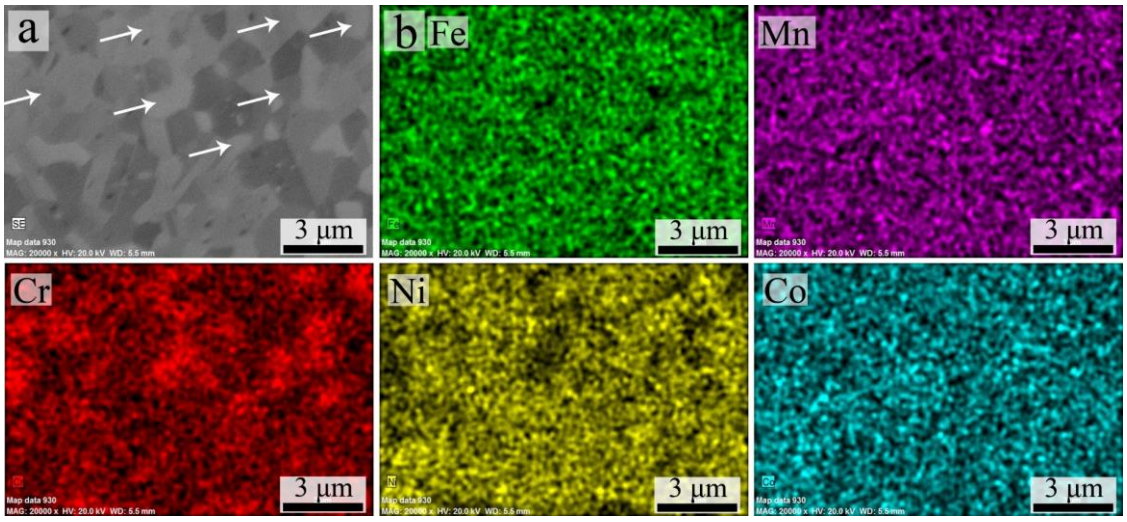

Figure 22. (a) The SEM-SE micrograph of the 850 ℃ specimen with (b) corresponding SEM-EDS maps representing the Cr-rich regions as sigma phases.

Figure 23a-d is illustrating the TEM micrograph of 850 ℃ sample for the zone without transformation-induced plasticity. The results are representing a Tetragonal (BCT) crystal structure (see Figure 23e) for sigma phases. The HRTEM-EDS result acquired from the center part of the micrograph is representing the sigma phase with a chromium-rich chemical composition. This sigma phase possesses a composition of 52Cr-26Fe-11Ni-8Mn-3Co at% which is aligned with the SEM-EDS results represented in Figure 22.

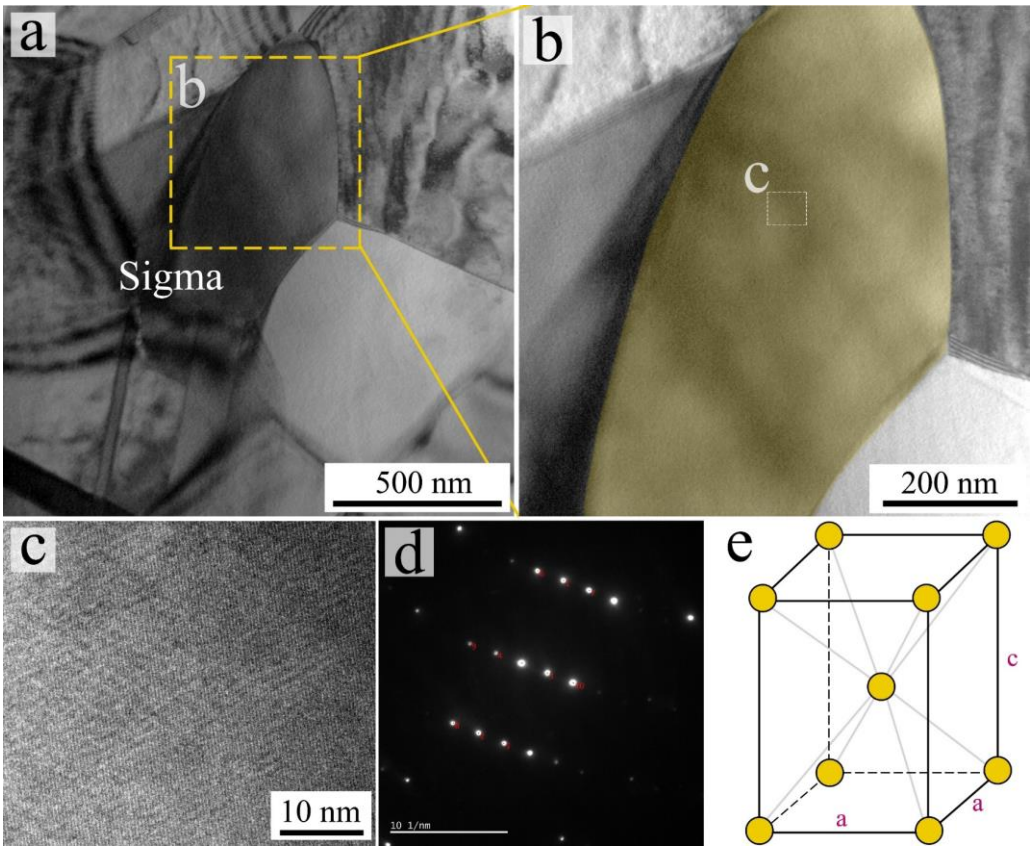

Figure 23. TEM micrographs for 850℃ post annealed sample at the zone without the TRIP mechanism (a and b) are representing TEM-micrographs including FCC, B2, and sigma phases, (c) HRTEM graph from the sigma phase, (d) SAED pattern of sigma phase, and (e) schematic of BCT for sigma phase.

4.2.3 Kernel average misorientation (KAM) analysis

Figure 24 indicates the KAM maps of the samples annealed at 750 ℃ and 850 ℃ at both the grip and tip parts. Inspection of the grip parts of these samples reveals that by increasing the post-deformation annealing temperature from 750 ℃ to 850 ℃, the KAM value decreases from 0.403º to 0.360º (Figure 24a and c). Also, collating the KAM values of the grip and tip parts of these samples presents a drastic increment for the latter. This can be attributed to the enhanced dislocation density in the grip part following tensile straining.

Similarly, the as-rolled specimen demonstrates a distinctly high KAM value of 1.688 (Figure 24f). It is also interesting to note that the KAM value of the tip part in the 850 ℃ sample is higher than that of the 750 ℃ sample, despite the lower KAM value of the former in the grip part, i.e., annealed condition. This can be related to the interaction of the sigma phase with the dislocation substructure, influencing the recovery dynamics [71].

According to the results represented in Figure 24, it is obvious that different thermo-mechanical processing routes can alter the KAM values. The evolution in KAM values can be linked to a change in intragranular dislocation density in the alloy structure. Based on the presented results, generated dislocations during cold rolling are recovered drastically after the post-deformation annealing treatments.

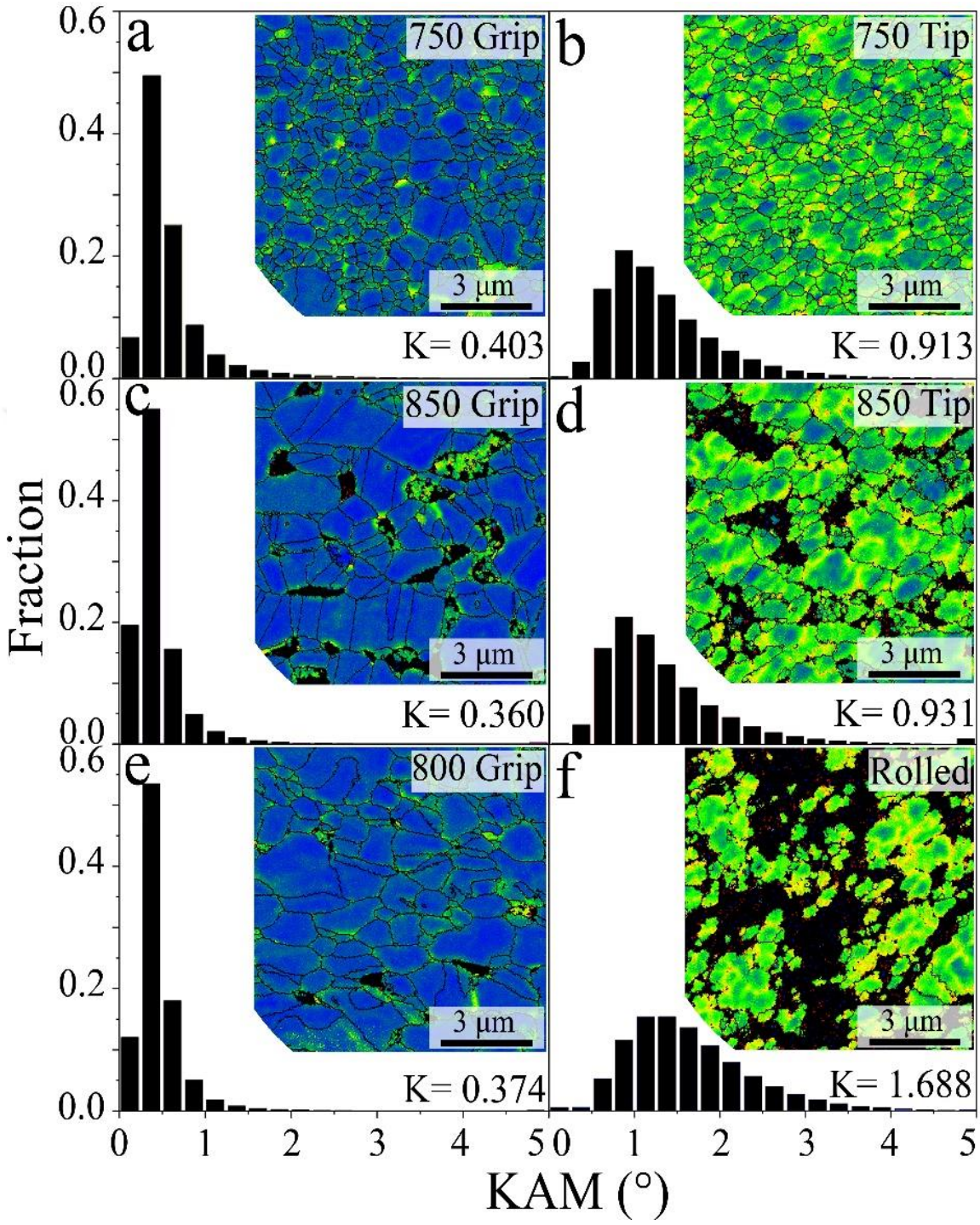

Figure 24. The Kernel average misorientation (KAM) maps of the samples annealed at (a) 750 ℃ taken from the grip part, (b) 750 ℃ taken from the tip part, (c) 850 ℃ taken from the grip part, (d) 850 ℃ taken from the tip part, (e) 800 ℃ taken from the grip part, and (f) the rolled specimen.

However, this reduction in dislocation density can be at a different level depending on the annealing temperature. In particular, the lattice misorientation is decreased by elevation in the annealing temperature. In other words, a higher portion of the deformation-induced strain remains in the sample annealed at 750℃, in contrast to other post-rolling annealed samples. However, the samples annealed at 800 ℃ and 850 ℃ show smaller KAM values representing a lower dislocation density, which implies a near-fully recrystallized microstructure for these conditions.

It can also be unveiled that after applying stress, the tip parts possess higher KAM levels. Specifically, a higher KAM value suggests a rising density of intragranular dislocations. In the absence of plastic deformation, the sample annealed at 750 ℃ has the highest presence of intragranular dislocations in the microstructure among the annealed samples. These intergranular dislocations which are initiated from partial annealing conditions may help strengthen the sample annealed at 750 ℃. However, near fully recrystallization conditions is dampening the strength of the annealed samples depending on the recrystallization level due to annealing temperature (Figure 24).

4.2.4 TEM Analysis

The matrix in stacking sequence of ABC in compact [111] plane of FCC crystal structure is changed for a twin to stacking sequence of CBA in same compact [111] plane. Figure 25 is representing the annealing twinning in the 850 ℃ sample and it is showing the stacking sequence of [111] planes at the twin boundary plane (represented in red color) on both sides of the coherent boundary plane. In this annealing twinning, a sequence of ABCABCABC is changed to ABCABACBA [102]. As illustrated in the HRTEM

micrographs (Figure 25) the twin boundaries represent a flat shape and a facetted appearance regarding their low energy grain boundaries.

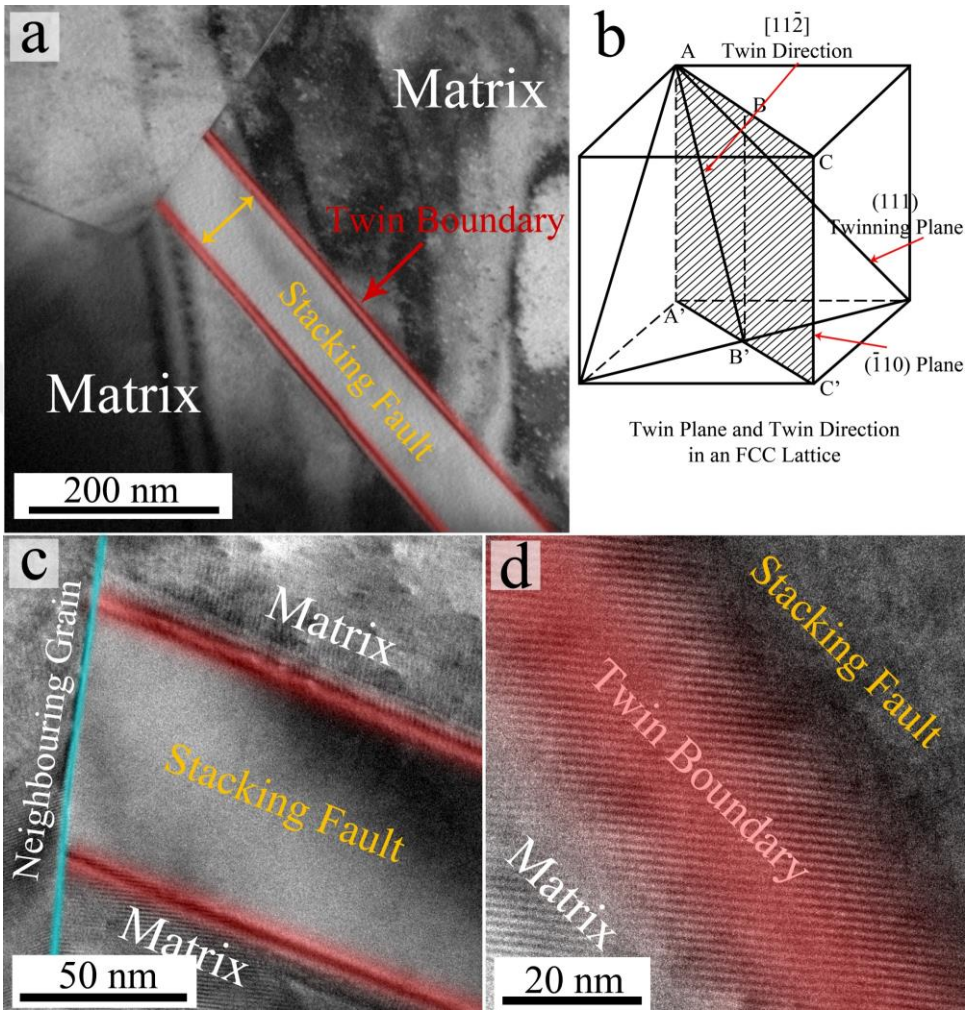

Figure 25. Annealing twins represented in fully recrystallized grains of 850 ℃ sample free of dislocations and schematic illustrating the present planes and directions in annealing twin in an FCC lattice.

It seems that the annealing twins should be more favorable in the 850 ℃ sample since the applied temperature during the annealing process is much higher than in the other circumstances. Most probably, the 850 ℃ sample possesses a higher chance of producing annealing twins in its structure. Obviously, applying a higher annealing temperature

increases the grain boundary velocity migration and intensifies the grains' incident probability [103]. Ever since the stacking fault energy is the same for all samples the annealing twin's production rate increases with increasing the annealing temperature.

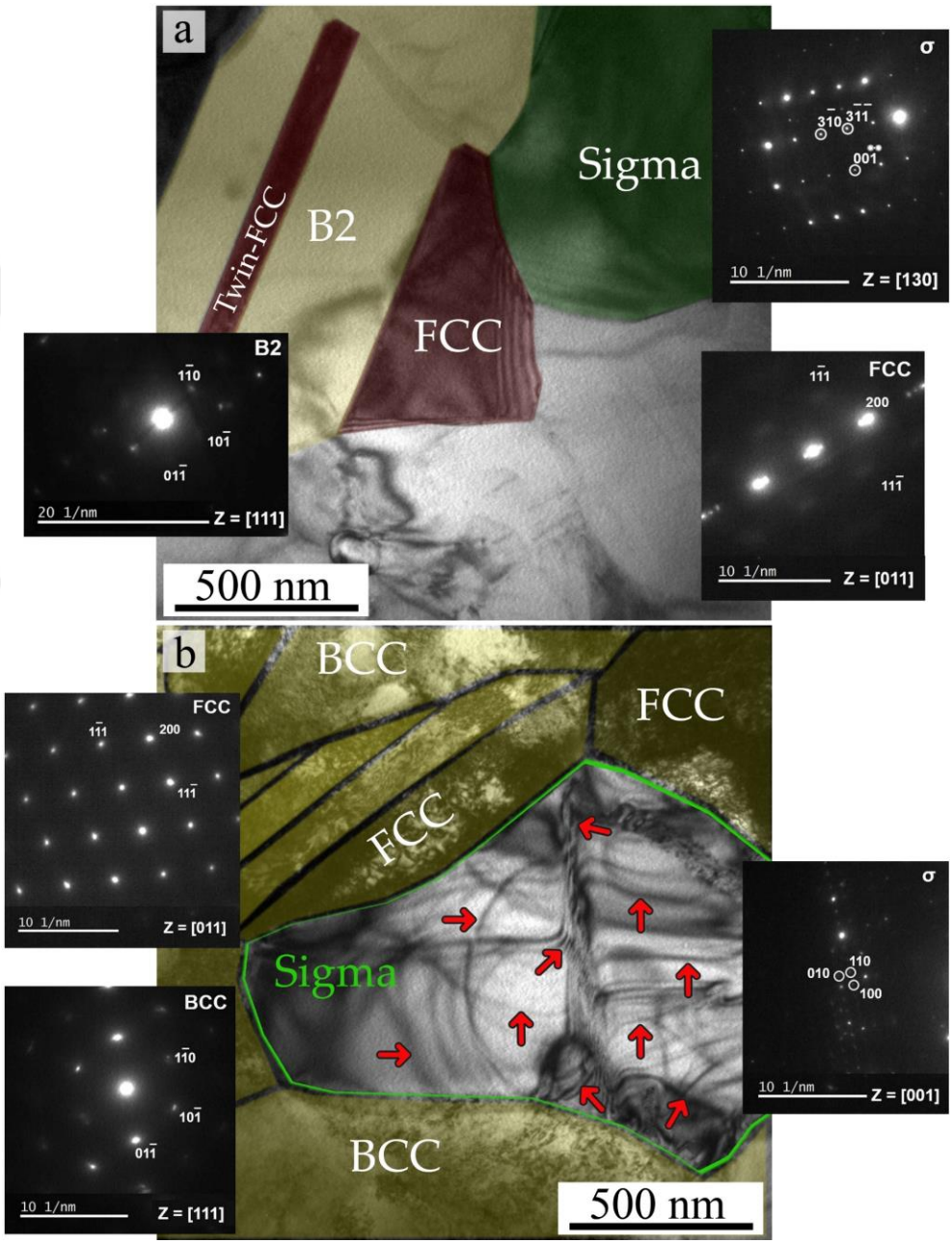

Figure 26. Transmission Electron Microscopy (TEM) micrograph of 850C (a) grip part possessing B2 crystal structure and (b) TRIP assisted zone (gage part) possessing BCC crystal structure with their related SAED pattern.

By analyzing TEM results for TRIP-assisted regions (near to necking area) four different phases can be detected. The FCC, B2, Sigma phases, and BCC (disordered crystal structure) are caused by the TRIP mechanism during plastic deformation. The TEM results illustrate no trace of BCC crystal structure in non-TRIP-assisted areas (Figure 26). As represented in the Figure 26b dislocations produced during plastic deformation in the microstructure and sigma phase also participated in this process with introducing dislocation (red arrows) in its structure.

Therefore, it can be confirmed that:

i. It seems that the TRIP mechanism has affected the microstructure by consuming the produced dislocation during plastic deformation due to present dislocation pile-ups in the phases (Figure 26b).
ii. The TRIP mechanism is not producing an ordered Body-centered cubic (B2) structure during plastic deformation since it introduced the Body-centered cubic (BCC) structure (Figure 26a).
iii. TRIP occurrence by introducing BCC crystal structure during plastic deformation boosts strain hardening in the necking area and postpones the rupture of the structure.

4.3 Mechanical properties

Figure 27a illustrates the engineering stress-strain curves of the as-received (homogenized), rolled, and post-deformation annealed samples. The as-received sample presents a YS of 172 MPa, a UTS of 442 MPa, and a total elongation of 43%, indicating a ductile mechanical behavior. After cold rolling, the YS and UTS of the sample enhance up

to 1157 MPa and 1259 MPa, respectively, with an expense in the total elongation reduction to 4.9%. After post-deformation annealing at 750 ℃, the YS reaches about 1 GPa with total elongation of about 10%. These values can be different if values are calculated by employing instantaneous area. The UTS values are shifting to higher amounts, however, the YS values stay constant due to constant cross-section (being in the elastic region) (see Figure 27b).

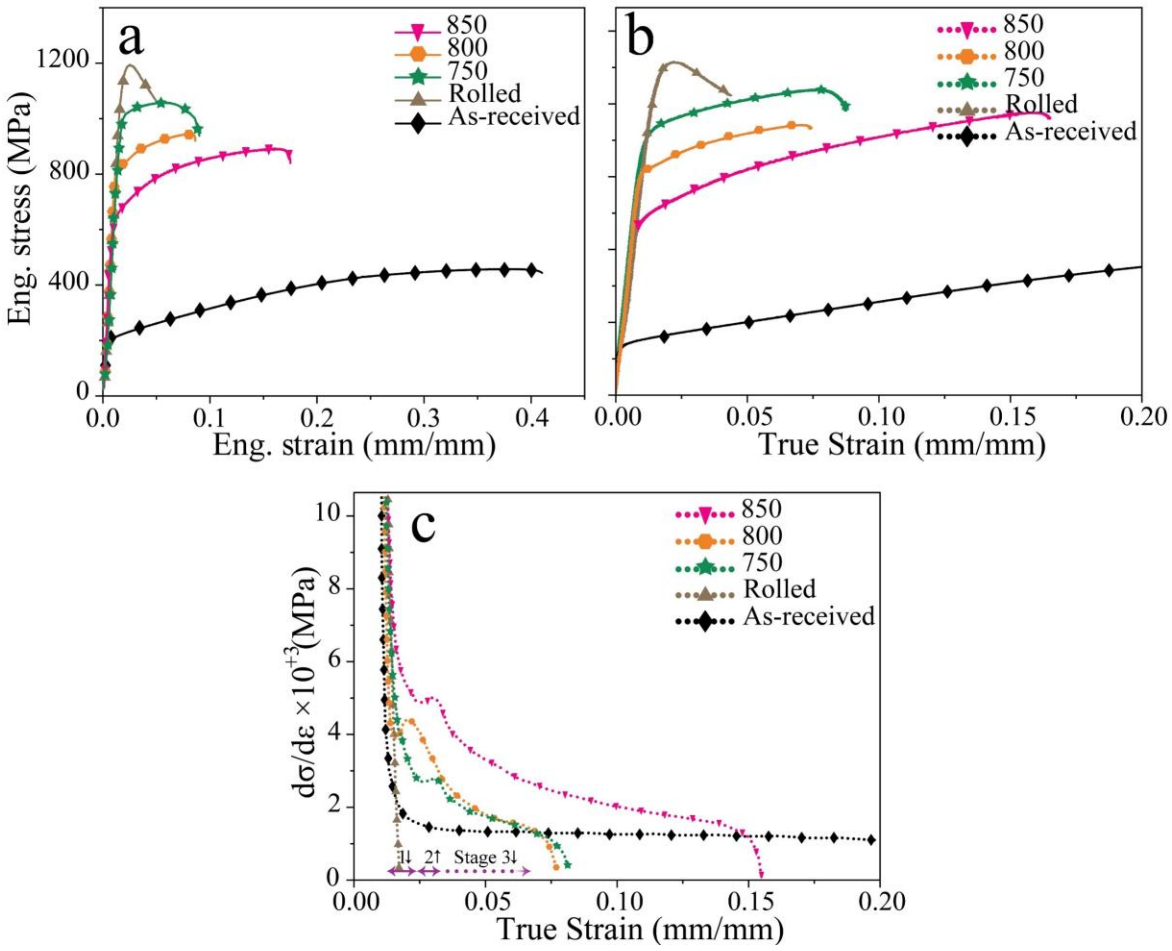

Figure 27. (a) Engineering stress-strain graph, (b) true stress-strain graph, and (c) strain hardening rate (SHR) curves of the present HEA at different processing conditions.

The stress-strain curves demonstrated a monotonous shift to lower stress levels by increasing the annealing temperature, though the ductility levels represent a noticeable improvement. According to the tensile results, the sample annealed at 750 ℃ exhibits about

6 times higher YS and UTS as compared with the as-received condition. Also, the sample annealed at 850 ℃ displays about 4 times higher elongation in comparison with the rolled sample. Hence, the post-rolling annealed samples present a trade-off mechanical performance that can be fine-tuned by the annealing condition.

The strain hardening rate (SHR) values are calculated for the samples using the following equation:

$$\Theta = \frac{d\sigma}{d\varepsilon} \quad (1)$$

where σ and ε are the true stress and strain, respectively.

According to the calculated SHR, the as-received sample shows a two-step behavior (Figure 27c). However, the rolled sample represents a single-step decrease without a sign of strain hardening during plastic deformation. In comparison, post-deformation annealed samples demonstrate a three-stage strain hardening behavior. The first stage shows a drastic decreasing trend which can be attributed to elastic to plastic transition.

At the second stage, the SHR curves represent an up-turn increment, and the third stage presents a continuous decreasing trend until the failure point. Moreover, close inspection of the SHR results reveals that the annealed samples possess a higher SHR as compared to the as-received and rolled samples. This is expected due to enhanced dislocation storage capacity brought about by recovery mechanisms [104].

The fracture surfaces of the as-received and post-rolling annealed samples are demonstrated in Figure 28a-f. As shown in Figure 28a, traces of ductile fracture are evident since deep and larger dimples can be observed for the as-received sample resulting in a high ductility of 43%. Moreover, larger dimples observed on the fracture surface of the as-received

material (Figure 28a and b) can be linked to the coarse-grained FCC structure of this condition (Figure 19d).

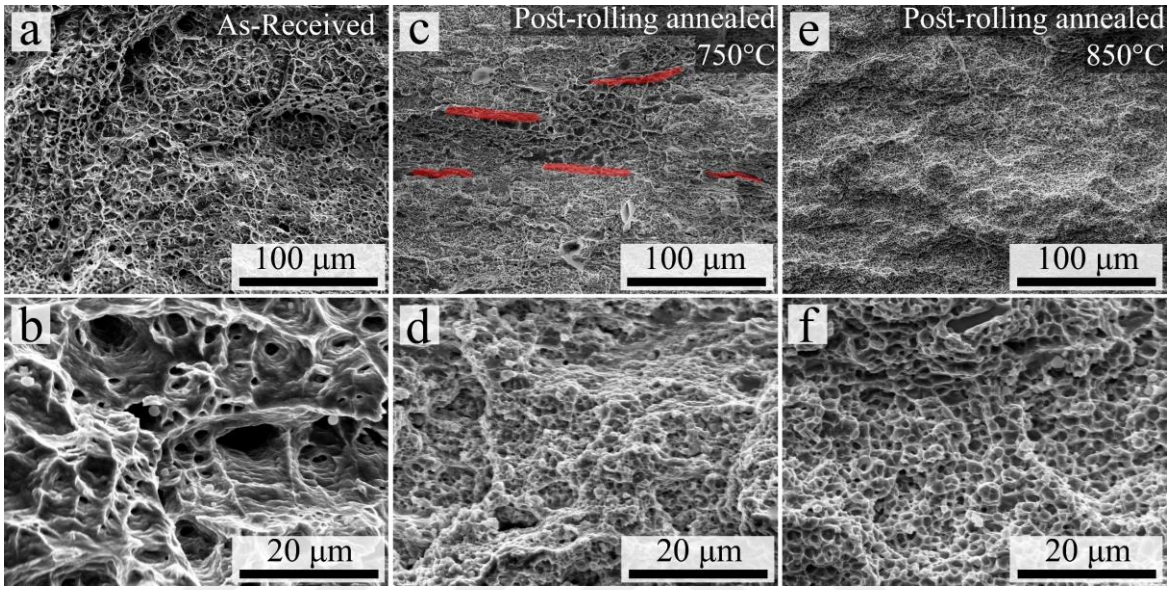

Figure 28. (a) Engineering stress-strain and (b) true stress-strain and strain hardening rate (SHR) curves of the present HEA at different processing conditions, and fracture surface of the samples at different conditions of (c and d) as-received, (e and f) annealed at 750 ℃, and (g and h) annealed at 850 ℃.

Shallow and smaller dimples in comparison to the as-received counterpart can be detected on the fracture surfaces captured for both 750 ℃ and 850 ℃ conditions (Figure 28c-f), being in line with the lower ductility of rolled samples [105–109]. Furthermore, as indicated by reddish marks in Figure 28c, the hardness mismatch between the FCC and the thermally induced (before tension) and the deformation-induced (during tension) BCC phases provided the sites with high potential of rupture and consequently decreased the strain to failure of the 750 ℃ sample. The same hardness mismatch shall also attest for the 850 ℃ sample as well, but to a lesser degree, as the propensity for FCC to BCC phase transformation is considerably lower.

4.4 Analysis of Structure-Property Relations

During plastic deformation, the TRIP mechanism can simultaneously modify the strength and ductility and drive more uniform plastic deformation by deferral of stress localization (necking) in the microstructure [110]. Therefore, TRIP considerably increases the work hardening in the localized stress zone and halts inhomogeneous plastic deformation [111–113]. It is also shown that with increasing post-rolling treatment temperature, the KAM values decrease in the samples. Moreover, the intragranular fracture can be delayed with the virtue of misorientation initiated from lattice distortion caused by a high dislocation density [114].

More likely, one of the underlying reasons for the postponement of failure in the 750 ℃ annealed sample could be the presence of remnant strain in the structure. Therefore, partial recovery of dislocations supports uniform plastic deformation and shifts necking to higher strain values in this condition.

TRIP plays a critical role in improving strain hardening and sustaining uniform plastic deformation. Thus, enhanced strain hardening can contribute as another reason to delaying the necking phenomenon and subsequently to stimulating tensile ductility [113]. The calculated SHR for all annealed conditions revealed a multi-step hardening rate due to the TRIP mechanism in the plastic region in all post-rolling annealed samples, and its occurrence is limited at the higher annealing temperatures of over 750 ℃.

A continuous increase in strain hardening is attributed to the introduction of the hard-domain (BCC) in the microstructure associated with the transformation shear stress [115]. Therefore, by comparing the tensile test results, it is demonstrated that introducing a suitable

microstructure for transformation-induced plasticity can lead to a superior mechanical behavior.

The development of various microstructures regarding the grain sizes and their distribution is another factor that considerably affects the mechanical behavior. Among the conditions, the 750 ℃ annealed has the smallest grain size distribution and thus is expected to exhibit the highest YS with low ductility [116,117]. Previous research indicates that finer grains activate more intragranular dislocations and intensify interactions with slip bands [72,115]. Furthermore, regarding the KAM results, the samples annealed at 750 ℃ possess the highest contribution of intragranular dislocations.

Therefore, due to the ability of phase transformation under plastic deformation coupled with the fine grain size and its favorable distribution, this thermo-mechanical processing route provides a decent combination of strength over 1 GPa and uniform elongation over 5% for the understudied HEA.

4.5 Mechanical behavior studies for 2nd composition

Figure 29 is representing the mechanical behavior of the 2nd composition under various annealing and aging conditions. The homogenized sample is representing a ductile behavior (engineering and true strain to failure of 58% and 47%, respectively) with high capability in strain hardening. The YS and UTS for this structure are about 483 and 744 MPa, respectively (see Figure 29a). However, analyzing the true stress-strain results (see Figure 29b) is showing that the YS and UTS values have intensified to 483 MPa and 1135 MPa, respectively. It is showing that the microstructure most likely possesses an FCC crystal structure with high distortion in its atomic crystal structure. The high distortion level can be

understood by possessing higher ductility besides higher YS and UTS values. Plus, comparing the δ values for two different studied compositions is showing that the δ values are modified from 4.1689% to 6.9565%. This increase in δ value is originated from the implemented early transition metals with higher atomic radii in the atomic crystal structure. This difference boosts the distortion level in the FCC crystal and increases strain to failure, YS, and UTS simultaneously.

Applying 80% reduction intensified the YS and UTS to 1604 MPa and 1619 MPa, respectively (engineering and true values are almost the same). However, it decreases the strain to failure from 58% to 5.6%. It seems that the microstructure possesses a high density of piled-up dislocations and there is no space for strain hardening since these two points have close values. Therefore, despite having high YS and UTS values the strain hardening ability is very low for this microstructure.

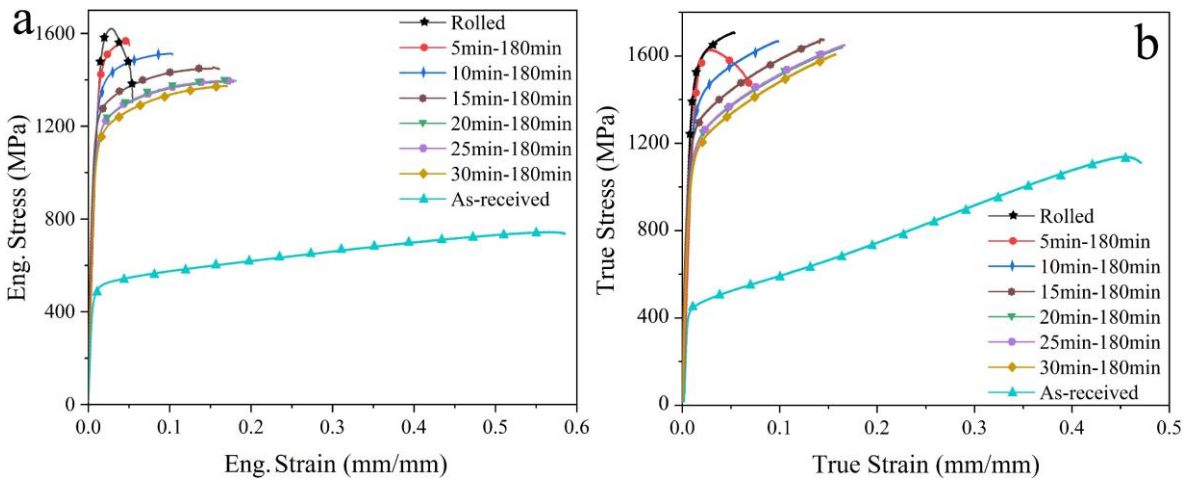

Figure 29. (a) Engineering stress-strain and (b) true stress-strain for as-received, rolled, and multiple annealing at 900 ℃ with the durations of 5, 10, 15, 20, 25, and 30 minutes followed by 180 minutes aging at 650 ℃ for 2nd composition.

Annealing followed by aging processes introduces an exceptional mechanical behavior for the alloy (see Figure 29). The results are demonstrating slight differences in mechanical behavior between annealed samples for a longer period of time (annealing for 20, 25, and 30 minutes). In addition, annealing for a longer time drops the YS and UTS values to unacceptable values. However, it seems that annealing for a shorter duration and aging for 180 minutes causes a partially recrystallized microstructure which is initiated from a partial recovery of dislocation and can lead to a lower strain hardening ability. Moreover, it seems (with comparing the true values) that all annealed-aged conditions can reach a similar UTS level around 1600 MPa with increasing strain by increasing the annealing temperature.

The results are showing that the 10min-180min and 15min-180min samples are the best samples for this composition. Each of these samples has its advantages but due to higher ductility (almost 20%) at GPa level stresses, the 15min-180min condition can be announced as the best condition for the 2nd composition. The 15min-180min sample possesses YS and UTS values of 1283 and 1457 MPa, respectively. This sample has a high capability of strain hardening in GPa level stresses which can be initiated from μ-precipitation, geometrically necessary dislocations (GNDs), high distorted atomic crystal structure, proper distribution of phases, and modified grains in the microstructure.

CHAPTER V

CONCLUSION

The current work depicts a systematic effort to investigate the effects of microstructural evolution on the mechanical behavior of a TRIP-assisted multi-phase high entropy alloys with the following conclusions.

i. The post-rolling annealing at 750 ℃ enhanced the yield strength to 1 GPa, which is almost up to six-folds higher as compared to the initial condition along with a decent ductility of about 10%.

ii. The degree of recrystallization played a critical role in the mechanical behavior of a TRIP-assisted multi-phase HEA. Intragranular dislocations can help demonstrate uniform plastic deformation at higher stress levels.

iii. The extent of TRIP mechanisms can be limited by increasing the sigma phase in the multi-phase HEA through the adjustment of thermo-mechanical processing parameters.

iv. The provision of moderate ductility at higher stress in the 750 ℃ annealed sample may be attributed to the synergistic deformation mechanisms involving dislocation slip and phase transformation, which maintain the ability of prolonged strain hardening.

v. Employing back- and forward-stress, pinning effect, and grain boundaries in combination can boost the mechanical behavior to GPa levels.

FUTURE WORKS

In the present work, it has been tried to dig in and study the mechanical behavior of a novel heterogeneous High Entropy Alloy at room temperature. But multiple areas can have great potential to carry on. Therefore, a few suggestions for future research works are listed.

1. The thermomechanical processes can be involved in different methods including free plastic deformation, which can introduce different textures in micron, submicron, and nano-level in the alloy structure.
2. The mechanical tests in this thesis were done at room temperature, however, studying the mechanical behavior of the designed heterogeneous MPEA at cryogenic temperature can be astonishing results. This composition due to the absence of precipitation in its structure is not recommended for studying in high temperatures.
3. Studying the effect of applied temperature during plastic deformation with focusing on the thermodynamic of the TRIP mechanism can be another hot topic for this composition and others with the capability of the TRIP mechanism.
4. The mechanical tests are highly recommended to study in different applied strain rates during plastic deformation. Investigating the TRIP mechanism under different tensile strain rates and how this mechanism takes effect from parameters except temperature can be interesting.
5. Studying the effect of back- and forward stress (employing geometrically necessary dislocations) and grain boundaries on the low cycle fatigue (LCF) behavior can be pursued.

BIBLIOGRAPHY

[1] B. Cantor, I.T.H. Chang, P. Knight, A.J.B. Vincent, Microstructural development in equiatomic multicomponent alloys, Mater. Sci. Eng. A. 375–377 (2004) 213–218.

[2] B.J. Yeh, S. Chen, S. Lin, J. Gan, T. Chin, T. Shun, C. Tsau, Nanostructured High-Entropy Alloys with Multiple Principal Elements : Novel Alloy Design Concepts and Outcomes, Adv. Eng. Mater. 6 (2004) 299–303.

[3] Y. Wei, Y. Li, L. Zhu, Y. Liu, X. Lei, G. Wang, Y. Wu, Z. Mi, J. Liu, H. Wang, H. Gao, Evading the strength-ductility trade-off dilemma in steel through gradient hierarchical nanotwins, Nat. Commun. 5 (2014).

[4] J.L. Cann, A. De Luca, D.C. Dunand, D. Dye, D.B. Miracle, H.S. Oh, E.A. Olivetti, T.M. Pollock, W.J. Poole, R. Yang, C.C. Tasan, Sustainability through alloy design: Challenges and opportunities, Prog. Mater. Sci. (2020) 100722.

[5] E.P. George, W.A. Curtin, C.C. Tasan, High entropy alloys: A focused review of mechanical properties and deformation mechanisms, Acta Mater. 188 (2020) 435–474.

[6] G.M. Tomboc, T. Kwon, J. Joo, K. Lee, High entropy alloy electrocatalysts: A critical assessment of fabrication and performance, J. Mater. Chem. A. 8 (2020) 14844–14862.

[7] J.W. Yeh, S.K. Chen, S.J. Lin, J.Y. Gan, T.S. Chin, T.T. Shun, C.H. Tsau, S.Y. Chang, Nanostructured high-entropy alloys with multiple principal elements: Novel alloy design concepts and outcomes, Adv. Eng. Mater. 6 (2004) 299–303.

[8] P. Asghari-Rad, P. Sathiyamoorthi, J.W. Bae, H. Shahmir, A. Zargaran, H.S. Kim, Effect of Initial Grain Size on Deformation Mechanism during High-Pressure Torsion in V10Cr15Mn5Fe35Co10Ni25 High-Entropy Alloy, Adv. Eng. Mater. 22 (2020) 1–9.

[9] B. Cantor, Multicomponent high-entropy Cantor alloys, Prog. Mater. Sci. (2020) 100754.

[10] E.P. George, D. Raabe, O.R. Ritchie, High-Entropy Alloys, Nat. Rev. Mater. 4 (2019) 515–534.

[11] P. Sharma, V.K. Dwivedi, S.P. Dwivedi, Development of high entropy alloys: A review, Mater. Today Proc. 43 (2021) 502–509.

[12] M. Yang, D. Yan, F. Yuan, P. Jiang, E. Ma, X. Wu, Dynamically reinforced heterogeneous grain structure prolongs ductility in a medium-entropy alloy with gigapascal yield strength, PNAS. 115 (2018) 7224–7229.

[13] E. Ma, X. Wu, Tailoring heterogeneities in high-entropy alloys to promote strength–ductility synergy, Nat. Commun. 10 (2019) 1–10.

[14] Y. Estrin, A. Vinogradov, Extreme grain refinement by severe plastic deformation: A wealth of challenging science, Acta Mater. 61 (2013) 782–817.

[15] P. Sathiyamoorthi, H.S. Kim, Progress in Materials Science High-entropy alloys with heterogeneous microstructure : Processing and mechanical properties, Prog. Mater. Sci. (2020) 100709.

[16] E. Bagherpour, N. Pardis, M. Reihanian, R. Ebrahimi, An overview on severe plastic deformation: research status, techniques classification, microstructure evolution, and applications, Int. J. Adv. Manuf. Technol. 100 (2019) 1647–1694.

[17] C.C. Koch, J. Narayan, The inverse Hall-Petch effect - Fact or artifact?, Mater. Res. Soc. Symp. - Proc. 634 (2001) 1–11.

[18] A.H. Chokshi, A. Rosen, J. Karch, H. Gleiter, On the validity of the hall-petch relationship in nanocrystalline materials, Scr. Metall. 23 (1989) 1679–1683.

[19] C. Huang, X. Peng, Y. Zhao, S. Weng, B. Yang, T. Fu, Flow strength limit of nanocrystalline tantalum predicted with molecular dynamics simulations, Mater. Sci. Eng. A. 738 (2018) 1–9.

[20] B.R. Kuhr, K.E. Aifantis, Interpreting the inverse Hall-Petch relationship and

capturing segregation hardening by measuring the grain boundary yield stress through MD indentation, Mater. Sci. Eng. A. 745 (2019) 107–114.

[21] J.W. Matthews, Accomodation of misfit between single-crystal films of β-cobalt and copper, Thin Solid Films. 5 (1970) 369–378.

[22] F.C. Frank, W.T. Read, Multiplication processes for slow moving dislocations, Phys. Rev. 79 (1950) 722–723.

[23] Y. Zhu, X. Wu, Perspective on hetero-deformation induced (HDI) hardening and back stress, Mater. Res. Lett. 7 (2019) 393–398.

[24] D.A. Hughes, N. Hansen, D.J. Bammann, Geometrically necessary boundaries , incidental dislocation boundaries and geometrically necessary dislocations, Scr. Mater. 48 (2003) 147–153.

[25] X.L. Wu, P. Jiang, L. Chen, J.F. Zhang, F.P. Yuan, Y.T. Zhu, Synergetic strengthening by gradient structure, Mater. Res. Lett. 2 (2014) 185–191.

[26] M. Yang, Y. Pan, F. Yuan, Y. Zhu, X. Wu, Back stress strengthening and strain hardening in gradient structure, 3831 (2016).

[27] M.X. Yang, F.P. Yuan, Q.G. Xie, Y.D. Wang, E. Ma, X.L. Wu, Acta Materialia Strain hardening in Fe e 16Mn e 10Al e 0 . 86C e 5Ni high speci fi c strength steel, 109 (2016) 213–222.

[28] Y. Ma, M. Yang, F. Yuan, X. Wu, A Review on Heterogeneous Nanostructures : A Strategy for Superior Mechanical Properties in Metals, Metals (Basel). 9 (2019) 598.

[29] X. Wu, P. Jiang, L. Chen, F. Yuan, Y.T. Zhu, Extraordinary strain hardening by gradient structure, PANS. 111 (2014) 7197–7101.

[30] R.A. Swalin, Thermodynamics of Solids, 2nd ed., Wiley, New York, 1991.

[31] R. Kozak, A. Sologubenko, W. Steurer, Single-phase high-entropy alloys - An overview, Zeitschrift Fur Krist. 230 (2015) 55–68.

[32] W. Steurer, Single-phase high-entropy alloys – A critical update, Mater. Charact. 162 (2020) 110179.

[33] N.T.C. Nguyen, P. Asghari-Rad, P. Sathiyamoorthi, A. Zargaran, C.S. Lee, H.S. Kim, Ultrahigh high-strain-rate superplasticity in a nanostructured high-entropy alloy, Nat. Commun. 11 (2020) 2736.

[34] H. Shahmir, T. Mousavi, J. He, Z. Lu, M. Kawasaki, T.G. Langdon, Microstructure and properties of a CoCrFeNiMn high-entropy alloy processed by equal-channel angular pressing, Mater. Sci. Eng. A. 705 (2017) 411–419.

[35] X.X. Wu, X.Y. San, X.G. Liang, Y.L. Gong, X.K. Zhu, Effect of stacking fault energy on mechanical behavior of cold-forging Cu and Cu alloys, Mater. Des. 47 (2013) 372–376.

[36] H. Yu, J. Zhang, W. Fang, R. Chang, X. Bai, J. Yan, X. Zhang, B. Liu, F. Yin, A brief review of metastable high-entropy alloys with transformation-induced plasticity, Mater. Sci. Technol. (United Kingdom). 36 (2020) 1893–1902.

[37] Z. Tang, S. Zhang, R. Cai, Q. Zhou, H. Wang, Designing High Entropy Alloys with Dual fcc and bcc Solid-Solution Phases: Structures and Mechanical Properties, Metall. Mater. Trans. A Phys. Metall. Mater. Sci. 50 (2019) 1888–1901.

[38] T.S. Reddy, I.S. Wani, T. Bhattacharjee, S.R. Reddy, R. Saha, P.P. Bhattacharjee, Severe plastic deformation driven nanostructure and phase evolution in a Al0.5CoCrFeMnNi dual phase high entropy alloy, Intermetallics. 91 (2017) 150–157.

[39] I.S. Wani, T. Bhattacharjee, S. Sheikh, I.T. Clark, M.H. Park, T. Okawa, S. Guo, P.P. Bhattacharjee, N. Tsuji, Cold-rolling and recrystallization textures of a nano-lamellar AlCoCrFeNi2.1 eutectic high entropy alloy, Intermetallics. 84 (2017) 42–51.

[40] C.J. Tong, Y.L. Chen, S.K. Chen, J.W. Yeh, T.T. Shun, C.H. Tsau, S.J. Lin, S.Y. Chang, Microstructure characterization of AlxCoCrCuFeNi high-entropy alloy system with multiprincipal elements, Metall. Mater. Trans. A Phys. Metall. Mater. Sci. 36 (2005) 881–893.

[41] C. Chen, S. Pang, Y. Cheng, T. Zhang, Microstructure and mechanical properties of Al20-xCr20+0.5xFe20Co20Ni20+0.5x high entropy alloys, J. Alloys Compd. 659 (2016) 279–287.

[42] C.M. Lin, H.L. Tsai, Evolution of microstructure, hardness, and corrosion properties of high-entropy Al0.5CoCrFeNi alloy, Intermetallics. 19 (2011) 288–294.

[43] M.R. Chen, S.J. Lin, J.W. Yeh, S.K. Chen, Y.S. Huang, C.P. Tu, Microstructure and properties of Al0.5CoCrCuFeNiTix (x = 0-2.0) high-entropy alloys, Mater. Trans. 47 (2006) 1395–1401.

[44] I.S. Wani, G.D. Sathiaraj, M.Z. Ahmed, S.R. Reddy, P.P. Bhattacharjee, Evolution of microstructure and texture during thermo-mechanical processing of a two phase Al0.5CoCrFeMnNi high entropy alloy, Mater. Charact. 118 (2016) 417–424.

[45] W. T, K. J, C. B, Microstructure and mechanical properties of FeCoNiCuAl high-entropy alloy prepared by microwave-assisted combustion synthesis, Fenmo Yejin Jishu/Powder Metall. Technol. 29 (2011) 435-438+442.

[46] R. Sharma, A. Roy, P.S. De, Equimolar AlCuFeMn: A novel oxidation resistant alloy, Intermetallics. 135 (2021) 107215.

[47] S.S. Mishra, A. Bajpai, K. Biswas, TiVCrNiZrFex High entropy alloy: Phase evolution,magnetic and mechanical properties, J. Alloys Compd. 871 (2021).

[48] Z.H. Cao, G.Y. Zhai, Y.J. Ma, L.P. Ding, P.F. Li, H.L. Liu, H.M. Lu, Y.P. Cai, G.J. Wang, X.K. Meng, Evolution of interfacial character and its influence on strain hardening in dual-phase high entropy alloys at nanoscale, Int. J. Plast. 145 (2021).

[49] Y. Li, C. Wang, D. Ma, X. Zeng, M. Liu, X. Jiang, Y.X. Leng, Nano dual-phase CuNiTiNbCr high entropy alloy films produced by high-power pulsed magnetron sputtering, Surf. Coatings Technol. 420 (2021) 127325.

[50] N. Liu, M. Xu, Y.Y. Qian, P.J. Zhou, Microstructure, phase stability, and oxidation resistance of (FeCoNi)60Al15Cr25−xTix high-entropy alloys, J. Alloys Compd. 870 (2021).

[51] Y. Zhang, T. Zuo, Y. Cheng, P.K. Liaw, High-entropy alloys with high saturation magnetization, electrical resistivity, and malleability, Sci. Rep. 3 (2013) 1–7.

[52] Y. Zhang, T.T. Zuo, Z. Tang, M.C. Gao, K.A. Dahmen, P.K. Liaw, Z.P. Lu,

Microstructures and properties of high-entropy alloys, Prog. Mater. Sci. 61 (2014) 1–93.

[53] Y.J. Hsu, W.C. Chiang, J.K. Wu, Corrosion behavior of FeCoNiCrCux high-entropy alloys in 3.5% sodium chloride solution, Mater. Chem. Phys. 92 (2005) 112–117.

[54] M.H. Tsai, Physical properties of high entropy alloys, Entropy. 15 (2013) 5338–5345.

[55] B. Ren, Z.X. Liu, D.M. Li, L. Shi, B. Cai, M.X. Wang, Effect of elemental interaction on microstructure of CuCrFeNiMn high entropy alloy system, J. Alloys Compd. 493 (2010) 148–153.

[56] H.P. Chou, Y.S. Chang, S.K. Chen, J.W. Yeh, Microstructure, thermophysical and electrical properties in AlxCoCrFeNi ($0 \leq x \leq 2$) high-entropy alloys, Mater. Sci. Eng. B Solid-State Mater. Adv. Technol. 163 (2009) 184–189.

[57] X.F. Wang, Y. Zhang, Y. Qiao, G.L. Chen, Novel microstructure and properties of multicomponent CoCrCuFeNiTix alloys, Intermetallics. 15 (2007) 357–362.

[58] X. Yang, Y. Zhang, P.K. Liaw, Microstructure and compressive properties of NbTiVTaAlx high entropy alloys, Procedia Eng. 36 (2012) 292–298.

[59] Y. Zhang, X. Yang, P.K. Liaw, Alloy design and properties optimization of high-entropy alloys, Jom. 64 (2012) 830–838.

[60] Y.J. Zhou, Y. Zhang, Y.L. Wang, G.L. Chen, Microstructure and compressive properties of multicomponent Alx(TiVCrMnFeCoNiCu)100-x high-entropy alloys, Mater. Sci. Eng. A. 454–455 (2007) 260–265.

[61] K. Zhang, Z. Fu, Effects of annealing treatment on phase composition and microstructure of CoCrFeNiTiAl x high-entropy alloys, Intermetallics. 22 (2012) 24–32.

[62] O.N. Senkov, G.B. Wilks, D.B. Miracle, C.P. Chuang, P.K. Liaw, Refractory high-entropy alloys, Intermetallics. 18 (2010) 1758–1765.

[63] T. Nagase, S. Anada, P.D. Rack, J.H. Noh, H. Yasuda, H. Mori, T. Egami, MeV electron-irradiation-induced structural change in the bcc phase of Zr-Hf-Nb alloy with

an approximately equiatomic ratio, Intermetallics. 38 (2013) 70–79.

[64] J.W. Yeh, S.Y. Chang, Y. Der Hong, S.K. Chen, S.J. Lin, Anomalous decrease in X-ray diffraction intensities of Cu-Ni-Al-Co-Cr-Fe-Si alloy systems with multi-principal elements, Mater. Chem. Phys. 103 (2007) 41–46.

[65] S. Varalakshmi, M. Kamaraj, B.S. Murty, Processing and properties of nanocrystalline CuNiCoZnAlTi high entropy alloys by mechanical alloying, Mater. Sci. Eng. A. 527 (2010) 1027–1030.

[66] C. Li, J.C. Li, M. Zhao, Q. Jiang, Effect of alloying elements on microstructure and properties of multiprincipal elements high-entropy alloys, J. Alloys Compd. 475 (2009) 752–757.

[67] O.N. Senkov, F. Zhang, J.D. Miller, Phase composition of a CrMo0.5NbTa0.5TiZr high entropy alloy: Comparison of experimental and simulated data, Entropy. 15 (2013) 3796–3809.

[68] C.-C. Hsieh, W. Wu, Overview of Intermetallic Sigma (σ) Phase Precipitation in Stainless Steels, ISRN Metall. 2012 (2012) 1–16.

[69] G. Laplanche, S. Berglund, C. Reinhart, A. Kostka, F. Fox, E.P. George, Phase stability and kinetics of σ-phase precipitation in CrMnFeCoNi high-entropy alloys, Acta Mater. 161 (2018) 338–351.

[70] K. Cho, Y. Fujioka, T. Nagase, H.Y. Yasuda, Grain refinement of non-equiatomic Cr-rich CoCrFeMnNi high-entropy alloys through combination of cold rolling and precipitation of σ phase, Mater. Sci. Eng. A. 735 (2018) 191–200.

[71] P. Asghari-Rad, P. Sathiyamoorthi, N. Thi-Cam Nguyen, J.W. Bae, H. Shahmir, H.S. Kim, Fine-tuning of mechanical properties in V10Cr15Mn5Fe35Co10Ni25 high-entropy alloy through high-pressure torsion and annealing, Mater. Sci. Eng. A. 771 (2020) 138604.

[72] P. Asghari-Rad, P. Sathiyamoorthi, J.W. Bae, J. Moon, J.M. Park, A. Zargaran, H.S. Kim, Effect of grain size on the tensile behavior of V10Cr15Mn5Fe35Co10Ni25 high entropy alloy, Mater. Sci. Eng. A. 744 (2019) 610–617.

[73] F. Otto, A. Dlouhý, K.G. Pradeep, M. Kuběnová, D. Raabe, G. Eggeler, E.P. George, Decomposition of the single-phase high-entropy alloy CrMnFeCoNi after prolonged anneals at intermediate temperatures, Acta Mater. 112 (2016) 40–52.

[74] E.J. Pickering, R. Muñoz-Moreno, H.J. Stone, N.G. Jones, Precipitation in the equiatomic high-entropy alloy CrMnFeCoNi, Scr. Mater. 113 (2016) 106–109.

[75] M. Herbig, D. Raabe, Y.J. Li, P. Choi, S. Zaefferer, S. Goto, Atomic-scale quantification of grain boundary segregation in nanocrystalline material, Phys. Rev. Lett. 112 (2013) 1–5.

[76] T.H. Ahn, C.S. Oh, D.H. Kim, K.H. Oh, H. Bei, E.P. George, H.N. Han, Investigation of strain-induced martensitic transformation in metastable austenite using nanoindentation, Scr. Mater. 63 (2010) 540–543.

[77] J. Miao, C.E. Slone, T.M. Smith, C. Niu, H. Bei, M. Ghazisaeidi, G.M. Pharr, M.J. Mills, The evolution of the deformation substructure in a Ni-Co-Cr equiatomic solid solution alloy, Acta Mater. 132 (2017) 35–48.

[78] C.E. Slone, S. Chakraborty, J. Miao, E.P. George, M.J. Mills, S.R. Niezgoda, In fluence of deformation induced nanoscale twinning and FCC-HCP transformation on hardening and texture development in medium- entropy CrCoNi alloy, Acta Mater. 158 (2018) 38–52.

[79] X. Ou, M. Song, Deformation mechanisms of mechanically induced phase transformations in iron, Comput. Mater. Sci. 162 (2019) 12–20.

[80] V. Bert, D. Julian, S. Indradev, D.D. Roger, Thermo-Mechanical Processing of Metallic Materials, Elsevier, 2007.

[81] H. Christian, L.-A. Barrales-Mora, From High-Manganese Steels to Advanced High-Entropy Alloys, (2019).

[82] K. Zhu, C. Mager, M. Huang, Effect of substitution of Si by Al on the microstructure and mechanical properties of bainitic transformation-induced plasticity steels, J. Mater. Sci. Technol. 33 (2017) 1475–1486.

[83] D. Suh, S. Park, C. Oh, S. Kim, Influence of partial replacement of Si by Al on the change of phase fraction during heat treatment of TRIP steels, 57 (2007) 1097–1100.

[84] C.S. Pande, M.A. Imam, B.B. Rath, Study of annealing twins in FCC metals and alloys, Metall. Trans. A, Phys. Metall. Mater. Sci. 21 A (1990) 2891–2896.

[85] L. Llanes, C. Laird, The role of annealing twin boundaries in the cyclic deformation of f.c.c. materials, Mater. Sci. Eng. A. 157 (1992) 21–27.

[86] R.L. Fullman, J.C. Fisher, Formation of Annealing Twins During Grain Growth, J. Appl. Phys. 22 (1951) 1350–1355.

[87] B.B. Rath, M.A. Imam, C.S. Pande, NUCLEATION AND GROWTH OF TWIN INTERFACES IN FCC METALS AND ALLOYS, 1 (2000) 61–66.

[88] U. Mizutani, THE HUME-ROTHERY RULES FOR STRUCTURALLY COMPLEX ALLOY PHASES, in: B. Ser. Complex Met. Alloy., 2010: pp. 323–399.

[89] A. Takeuchi, A. Inoue, Quantitative evaluation of critical cooling rate for metallic glasses, Mater. Sci. Eng. A. 304–306 (2001) 446–451.

[90] Y. Zhang, Y.J. Zhou, J.P. Lin, G.L. Chen, P.K. Liaw, Solid-solution phase formation rules for multi-component alloys, Adv. Eng. Mater. 10 (2008) 534–538.

[91] B.S. Murty, J.W. Yeh, S. Ranganathan, High Entropy Alloys, 1st ed., 2014.

[92] S. Fang, X. Xiao, L. Xia, W. Li, Y. Dong, Relationship between the widths of supercooled liquid regions and bond parameters of Mg-based bulk metallic glasses, J. Non. Cryst. Solids. 321 (2003) 120–125.

[93] G. Hakan, Z. Mohsen, A novel medium entropy alloy based on iron-manganese-aluminum-nickel: Influence of boron addition on phase formation, microstructure, and mechanical properties, Mater. Res. Express. 7 (2019).

[94] D. Liang, C. Zhao, W. Zhu, P. Wei, F. Jiang, Y. Zhang, Q. Sun, F. Ren, Overcoming the strength-ductility trade-off via the formation of nanoscale Cr-rich precipitates in an ultrafine-grained FCC CrFeNi medium entropy alloy matrix, Mater. Sci. Eng. A. 762 (2019) 138107.

[95] A. Takeuchi, A. Inoue, Classification of Bulk Metallic Glasses by Atomic Size Difference , Heat of Mixing and Period of Constituent Elements and Its Application to Characterization of the Main Alloying Element, 46 (2005).

[96] H. Watanabe, T. Murata, S. Nakamura, N. Ikeo, T. Mukai, K. Tsuchiya, Effect of cold-working on phase formation during heat treatment in CrMnFeCoNi system high-entropy alloys with Al addition, J. Alloys Compd. 872 (2021) 159668.

[97] P. Asghari-Rad, P. Sathiyamoorthi, N.T.C. Nguyen, A. Zargaran, T.S. Kim, H.S. Kim, A powder-metallurgy-based fabrication route towards achieving high tensile strength with ultra-high ductility in high-entropy alloy, Scr. Mater. 190 (2021) 69–74.

[98] X. Wu, D. Mayweg, D. Ponge, Z. Li, Microstructure and deformation behavior of two TWIP/TRIP high entropy alloys upon grain refinement, Mater. Sci. Eng. A. 802 (2021) 140661.

[99] H. Kwon, J. Moon, J.W. Bae, J.M. Park, S. Son, H.S. Do, B.J. Lee, H.S. Kim, Precipitation-driven metastability engineering of carbon-doped CoCrFeNiMo medium-entropy alloys at cryogenic temperature, Scr. Mater. 188 (2020) 140–145.

[100] J. Gurland, A structural approach to the yield strength of two-phase alloys with coarse microstructures, Mater. Sci. Eng. 40 (1979) 59–71.

[101] Y. Yin, Q. Tan, Q. Sun, W. Ren, J. Zhang, S. Liu, Y. Liu, M. Bermingham, H. Chen, M.X. Zhang, Heterogeneous lamella design to tune the mechanical behaviour of a new cost-effective compositionally complicated alloy, J. Mater. Sci. Technol. 96 (2022) 113–125.

[102] T. Baudin, A.L. Etter, R. Penelle, Annealing twin formation and recrystallization study of cold-drawn copper wires from EBSD measurements, Mater. Charact. 58 (2007) 947–952.

[103] D. Poddar, A. Chakraborty, R.K. B., Annealing twin evolution in the grain-growth stagnant austenitic stainless steel microstructure, Mater. Charact. 155 (2019) 109791.

[104] H. Fan, Q. Wang, J.A. El-Awady, D. Raabe, M. Zaiser, Strain rate dependency of dislocation plasticity, Nat. Commun. 12 (2021) 1–11.

[105] A. Hosseinzadeh, G.G. Yapici, High temperature characteristics of Al2024/SiC metal matrix composite fabricated by friction stir processing, Mater. Sci. Eng. A. 731 (2018) 487–494.

[106] A. Hosseinzadeh, G.G. Yapici, On the high-temperature flow response of friction stir processed magnesium metal matrix composites, J. Eng. Mater. Technol. Trans. ASME. 143 (2021) 1–9.

[107] G. Moeini, S. V. Sajadifar, T. Wegener, C. Rössler, A. Gerber, S. Böhm, T. Niendorf, On the influence of build orientation on properties of friction stir welded Al-Si10Mg parts produced by selective laser melting, J. Mater. Res. Technol. 12 (2021) 1446–1460.

[108] J. CHEN, W. HOU, X. WANG, S. CHU, Z. YANG, Microstructure, porosity and mechanical properties of selective laser melted AlSi10Mg, Chinese J. Aeronaut. 33 (2020) 2043–2054.

[109] J. Zhang, H. Qiu, H. Zhu, Z. Xie, Effect of Al additions on the microstructures and tensile properties of AlxCoCr3Fe5Ni high entropy alloys, Mater. Charact. 175 (2021) 111091.

[110] Z. Li, C.C. Tasan, K.G. Pradeep, D. Raabe, A TRIP-assisted dual-phase high-entropy alloy: Grain size and phase fraction effects on deformation behavior, Acta Mater. 131 (2017) 323–335.

[111] W. Bleck, X. Guo, Y. Ma, The TRIP Effect and Its Application in Cold Formable Sheet Steels, Steel Res. Int. 88 (2017) 35–45.

[112] F.D. Fischer, G. Reisner, E. Werner, K. Tanaka, G. Cailletaud, T. Antretter, New view on transformation induced plasticity (TRIP), Int. J. Plast. 16 (2000) 723–748.

[113] M. Soleimani, A. Kalhor, H. Mirzadeh, Transformation-induced plasticity (TRIP) in advanced steels: A review, Mater. Sci. Eng. A. 795 (2020) 140023.

[114] T. Watanabe, S. Tsurekawa, Control of brittleness and development of desirable mechanical properties in polycrystalline systems by grain boundary engineering, Acta Mater. 47 (1999) 4171–4185.

[115] A.K. De, J.G. Speer, D.K. Matlock, D.C. Murdock, M.C. Mataya, R.J. Comstock, Deformation-induced phase transformation and strain hardening in type 304 austenitic stainless steel, Metall. Mater. Trans. A Phys. Metall. Mater. Sci. 37 (2006) 1875–1886.

[116] W. Qin, J. Li, Y. Liu, J. Kang, L. Zhu, D. Shu, P. Peng, D. She, D. Meng, Y. Li, Effects of grain size on tensile property and fracture morphology of 316L stainless steel, Mater. Lett. 254 (2019) 116–119.

[117] S. Kheiri, H. Mirzadeh, M. Naghizadeh, Tailoring the microstructure and mechanical properties of AISI 316L austenitic stainless steel via cold rolling and reversion annealing, Mater. Sci. Eng. A. 759 (2019) 90–96.

VITA

Amin Radi received the B.Sc. degree in Materials Science from the Sahand University of Technology, Tabriz, Iran, in 2013. He is currently working toward the M.Sc. degree as a research assistant under the supervision of Professor Guney Guven Yapici in the Mechanical Engineering department within MEMFIS at Özyeğin University, Istanbul, Turkey. His main research interests include the design and fabrication of Multi-principal Element Alloys (MPEAs).